Multiparameter bifurcations and mixed-mode oscillations in Q-switched CO_2 lasers

Eusebius J. Doedel[1] and Carlos L. Pando L.[2]

[1]*Department of Computer Science, Concordia University, 1455 Boulevard de Maisonneuve Ouest, Montréal, Québec, Canada H3G 1M8*

[2]*Instituto de Física, Benemérita Universidad Autónoma de Puebla, Apartado Postal J-48, Puebla 72570, México*

(Received 10 December 2013; published 9 May 2014)

We study the origin of mixed-mode oscillations and related bifurcations in a fully molecular laser model that describes CO_2 monomode lasers with a slow saturable absorber. Our study indicates that the presence of isolas of periodic mixed-mode oscillations, as the pump parameter and the cavity-frequency detuning change, is inherent to Q-switched CO_2 monomode lasers. We compare this model, known as the dual four-level model, to the more conventional 3:2 model and to a CO_2 laser model for fast saturable absorbers. In these models, we find similarities as well as qualitative differences, such as the different nature of the homoclinic tangency to a relevant unstable periodic orbit, where the Gavrilov-Shilnikov theory and its extensions may hold. We also show that there are isolas of periodic mixed-mode oscillations in a model for CO_2 lasers with modulated losses, as the pump parameter varies. The coarse-grained bifurcation diagrams of the periodic mixed-mode oscillations in these models suggest that these oscillations belong to similar classes.

DOI: 10.1103/PhysRevE.89.052904 PACS number(s): 05.45.−a, 42.60.Gd, 42.60.Mi, 42.65.Sf

I. INTRODUCTION

Certain dynamical systems display multiple time scales and are the subject of substantial current research [1,2]. These are known as mixed-mode oscillators (MMOs), and their evolution switches between slow and fast motions and small and large amplitudes. MMOs are ubiquitous in nature and have been observed for over 30 years in chemical, physical, biological, and engineering systems [1,2]; in particular in chemical reactions [3], neural systems [4], intracellular calcium dynamics [5], lasers [6], dusty plasmas [7], and Faraday waves in fluids [8].

Recent work gives improved insight into the mathematical properties of MMOs. In Ref. [2], a systematic framework is considered for studying the properties of MMOs, where numerical methods for computing invariant manifolds and their intersections are an important tool. Singular Hopf bifurcation has been identified as one mechanism for the creation of mixed-mode oscillations [9]. Many slow-fast systems show that there is a range of parameter values for which the model has MMOs, which have also been explained in terms of the canard phenomenon [10].

Recently, we have studied laser models described by nonlinear ordinary differential equations (ODE) systems with fast and slow variables, i.e., some of the derivatives are multiplied by a small parameter. Using a suitable reduction procedure, we found that reduced models preserve the bifurcation structure qualitatively quite well. These reduced systems have one fast variable, the laser intensity, and two or three slow variables, namely, the energy level populations [11–13]. Numerical continuation was used to explore regions in parameter space where MMOs exist.

In this article, we consider another laser model that belongs to the category of mixed-mode oscillators: the dual four-level model (4:4 model) for the CO_2 laser with a slow saturable absorber. Motivated by the physics of this model and the renewed interest in MMOs, we investigate its dynamics using numerical continuation and supplemental simulations. We also give a comparison to related models and discuss the connection of our results to experiments.

A. The physics and dynamics of the CO_2 laser with a saturable absorber

In Q-switched lasers, the optical resonator losses are changed from high values (low Q factor) to low values (high Q factor) after the pump energy has been stored long enough in the active medium. Q switching has been achieved in different laser gain media, such as ion-doped solid-state crystals and semiconductor media and gas mixtures [14]. Much theoretical and experimental work concentrated on an important Q-switched laser: the CO_2 laser with intracavity gaseous saturable absorbers [15–18]. Its rich dynamical behavior and its versatility in changing control parameters have made it a particularly interesting object for study in nonlinear dynamics [17–30].

Our study considers a theoretical model of the CO_2 laser with saturable absorber (LSA) where the intracavity gaseous saturable absorber is an SF_6 gas mixture [21,22]. This model has also been used when the amplifier and absorber contain other mixtures of gases [21,22]. It is known as the dual four-level model (4:4 model), where the amplifier and absorber are both described by four-level models [20,21], composed of two active rotational states and two reservoir states.

The central contribution of our article is a study of the relevant bifurcations of passive Q-switched (PQS) self-pulsations in the 4:4 model, as physically relevant control parameters are varied. Each PQS self-pulsation of the CO_2 LSA typically consists of a leading spike, named the reinjection, and $n-1$ small intensity undulations in a tail [23,24]. In this article, we denote these periodic PQS self-pulsations as $\Pi^{(n)}$. When the incoherent external pump [27,31] or the cavity-frequency detuning [30] is changed in the experiment, period-adding cascades of PQS self-pulsations can arise: $\Pi^{(n)} \to \Pi^{(n+1)}$, or vice versa. In this paper, we show that the period-adding cascades of PQS self-pulsations can also be described within the framework of the 4:4 model. This is in contrast to the common belief that the 4:4 model does not predict the $\Pi^{(n)}$ observed in experiments [27,31]. Specifically, using numerical continuation methods [32], we show that the 4:4 model predicts the existence of isolas of periodic PQS self-pulsations $\Pi^{(n)}$ as

the incoherent external pump or the cavity-frequency detuning changes. By an *isola*, we mean a smooth, closed, and isolated family of periodic orbits, stable or unstable, which is generated as a single control parameter is free to change. Isolas of periodic orbits in autonomous systems have been found in different contexts, such as in an electronic circuit [33] and in a model for air oxidation of hydrogen in a continuous-flow stirred tank reactor [34,35]. We show that as the incoherent pump or the cavity-frequency detuning are changed, the origin of the period-adding cascades stems from the coexistence of stable $\Pi^{(n)}$. For each n, stable and unstable $\Pi^{(n)}$ belong to a corresponding isola $\mathcal{I}_n$, while their period increases with n. Previous studies of period-adding cascades have been done for optically injected lasers [36–38] and for a laser rate equation model with a term describing a saturable absorber and a modulated pump source [39].

In addition to this model, we also consider the more conventional 3:2 model [12], which is a generalization of the two-level rate-equation model for the CO_2 LSA, taking into account the presence of a third level in the active medium [23,27]. This model has *ad hoc* parameters that describe the temporal dynamics of this laser system very well [24,30]. We also discuss a CO_2 laser model for fast saturable absorbers, and we compare the models.

B. Main result and outline

Our study shows that isolas of periodic mixed-mode oscillations are inherent to Q-switched CO_2 monomode lasers, as the incoherent external pump or the cavity-frequency detuning changes. In addition to the LSA models, we show that a model for CO_2 lasers with modulated losses also has isolas of periodic MMOs as the pump parameter changes. To our knowledge, such isolas have not been reported earlier for PQS semiconductor lasers [40,41] or in PQS microchip lasers [42]. Despite the fact that the 4:4 model was devised a long time ago [20–22], its bifurcation structure has not been thoroughly studied, in contrast to the more popular model 3:2 model [23–31]. In this paper, we carry out this study and give a comparison to related LSA models, where we find qualitative similarities and differences. In particular, though the coarse-grained picture of the bifurcation diagrams is qualitatively similar, the relative position of the largest stability intervals along the isolas is different between the molecular models and the 3:2 model, as we change a second physical parameter such as the saturability.

This paper is organized as follows. In Sec. II, we discuss the 4:4 model at exact resonance, also considering the effect of the cavity-frequency detuning within the framework of semiclassical laser theory. In Sec. III, we compare the 4:4 model to its reduced version as the pump parameter changes at zero cavity-frequency detuning, emphasizing the onset of isolas. In Sec. IV, we consider a reduced version of the 4:4 model, as several physically relevant control parameters are varied, namely, the incoherent pump, the cavity-frequency detuning, the saturability, and the pressure in the absorber cell. Throughout we compare our results to those found in the literature in order to stress that the 4:4 model gives a good description of well-known experimental facts. In Sec. V, we consider bifurcation sequences near folds of isolas in the 4:4, 3:2, and 4:2 models. These occur near the homoclinic tangency to a relevant unstable periodic orbit along the primary periodic family in these models. In Sec. VI, we consider a physically different Q-switched monomode laser, namely, a molecular model for the CO_2 laser with modulated losses, where we show the existence of isolas of periodic MMOs as the pump parameter changes. In Sec. VII, we state our final conclusions. For completeness, we give the equations of the 3:2 and 4:2 model in the Appendix.

II. THE DUAL FOUR-LEVEL MODEL

In contrast to standard laser models, where a single mode interacts with a resonant atomic transition, in the CO_2 LSA the population transfers are more complicated since the amplifier and absorber cells each need to be modeled by a four-level system [21]. This model is known as the dual four-level model (4:4 model) [23,27]. In the early 1990s, a four-level model (4LM) was used to describe the amplifier in a CO_2 laser with modulated losses [43,44], for the CO_2 laser transient behavior [45,46], and for the CO_2 laser with electronic feedback [47–49]. Good quantitative agreement between models and experiments was found as parameters were varied. The saturable absorber of our system was described by a 4LM in 1971 [20,50]. Using this model, the transmission of CO_2 LSA self-pulsations through SF_6 gas mixtures was studied numerically in Ref. [50], which compared well with experiments. The factor determining the rate of absorption was shown to be the rotational energy transfer process between the resonant and nonresonant rotational levels from the same vibrational band [50].

A. The zero cavity-frequency detuning: Exact resonance

The 4:4 model is based on the usual field-matter equations in a resonant cavity [18]. Taking into account the dynamics of the active rotational states and the two reservoir states at exact resonance between the cavity and the molecular frequencies of the media, the coupled field-matter rate equations for a single-mode CO_2 LSA are described by the following set of equations [21,22]:

$$
\begin{aligned}
\frac{dI}{dt} &= -KI + \frac{B_g l_g}{L} I(N_2 - N_1) - \frac{B_a l_a}{L} I(\bar{N}_2 - \bar{N}_1),\\
\frac{dN_2}{dt} &= -B_g I(N_2 - N_1) - \gamma_2 N_2 - \gamma_R N_2 + \gamma_R' M_2 + \gamma_2 Q,\\
\frac{dN_1}{dt} &= B_g I(N_2 - N_1) - \gamma_1 N_1 - \gamma_R N_1 + \gamma_R' M_1,\\
\frac{dM_2}{dt} &= -\gamma_2 M_2 + \gamma_R N_2 - \gamma_R' M_2 + \gamma_2 z Q,\\
\frac{dM_1}{dt} &= -\gamma_1 M_1 + \gamma_R N_1 - \gamma_R' M_1,\\
\frac{d\bar{N}_2}{dt} &= -B_a I(\bar{N}_2 - \bar{N}_1) - \bar{\gamma}_2 \bar{N}_2 - \bar{\gamma}_R \bar{N}_2 + \bar{\gamma}_R' \bar{M}_2,\\
\frac{d\bar{N}_1}{dt} &= B_a I(\bar{N}_2 - \bar{N}_1) - \bar{\gamma}_1 \bar{N}_1 - \bar{\gamma}_R \bar{N}_1 + \bar{\gamma}_R' \bar{M}_1 + \bar{\gamma}_1 \bar{Q},\\
\frac{d\bar{M}_2}{dt} &= -\bar{\gamma}_2 \bar{M}_2 + \bar{\gamma}_R \bar{N}_2 - \bar{\gamma}_R' \bar{M}_2,\\
\frac{d\bar{M}_1}{dt} &= -\bar{\gamma}_1 \bar{M}_1 + \bar{\gamma}_R \bar{N}_1 - \bar{\gamma}_R' \bar{M}_1 + \bar{\gamma}_1 \bar{z} \bar{Q}.
\end{aligned}
\tag{1}
$$

Here, I is the field intensity within the laser cavity, and N_2 (M_2) and N_1 (M_1) denote the populations of the upper and lower active (reservoir) rotational energy levels in the gain medium, respectively. B_g and B_a are the cross sections multiplied by the velocity of light for the induced emission in the gain medium and in the absorber. Q is the incoherent pump induced by the excitation current in the gain medium. The parameters l_g and L are the lengths of the gain medium and laser cavity, l_a denotes the length of the absorption cell, K is the cavity loss rate, and z is the effective number of reservoir rotational levels in each vibrational band. Also, γ_R' is the rotational relaxation rate for the transitions between $M_2 \to N_2$ and $M_1 \to N_1$, and γ_R is the rotational relaxation rate for the inverse transitions, $\gamma_R/\gamma_R' = z$. The vibrational relaxation rates for N_1 and N_2 are denoted by γ_1 and γ_2. These relaxation rates hold also for M_1 and M_2. The same physical processes that take place in the active medium occur also in the absorber. In our notation, constants and variables with a bar are for the absorber and have the same meaning as those for the amplifier. The main difference with the amplifier is that in the absorber, the rotational energy levels of the upper energy vibrational band are not pumped, and there is never population inversion.

After normalization of the variables and parameters in Eq. (1), we obtain the following set of equations from the 4:4 model, which we call the complete model (CM) at exact resonance:

$$\begin{aligned}
\frac{dI}{dt} &= -I + I(N_2 - N_1) + \alpha I(\bar{N}_2 - \bar{N}_1),\\
\frac{dN_2}{dt} &= -I(N_2 - N_1) - \gamma_2 N_2 - \gamma_R N_2 + \gamma_R' M_2 + \gamma_2 Q,\\
\frac{dN_1}{dt} &= I(N_2 - N_1) - \gamma_1 N_1 - \gamma_R N_1 + \gamma_R' M_1,\\
\frac{dM_2}{dt} &= -\gamma_2 M_2 + \gamma_R N_2 - \gamma_R' M_2 + \gamma_2 z Q,\\
\frac{dM_1}{dt} &= -\gamma_1 M_1 + \gamma_R N_1 - \gamma_R' M_1,\\
\frac{d\bar{N}_2}{dt} &= -\beta I(\bar{N}_2 - \bar{N}_1) - \bar{\gamma}_2 \bar{N}_2 - \bar{\gamma}_R \bar{N}_2 + \bar{\gamma}_R' \bar{M}_2,\\
\frac{d\bar{N}_1}{dt} &= \beta I(\bar{N}_2 - \bar{N}_1) - \bar{\gamma}_1 \bar{N}_1 - \bar{\gamma}_R \bar{N}_1 + \bar{\gamma}_R' \bar{M}_1 + \bar{\gamma}_1,\\
\frac{d\bar{M}_2}{dt} &= -\bar{\gamma}_2 \bar{M}_2 + \bar{\gamma}_R \bar{N}_2 - \bar{\gamma}_R' \bar{M}_2,\\
\frac{d\bar{M}_1}{dt} &= -\bar{\gamma}_1 \bar{M}_1 + \bar{\gamma}_R \bar{N}_1 - \bar{\gamma}_R' \bar{M}_1 + \bar{\gamma}_1 \bar{z}.
\end{aligned} \tag{2}$$

Here, I denotes the intensity, which has been normalized by $I \to I B_g/K$. The populations and the pump variable Q in the gain medium have been rescaled identically, e.g., $Q \to Q B_g l_g/KL$. Relaxation parameters in the amplifier and absorber have also been normalized, e.g., $\gamma_1 \to \gamma_1/K$. Time has been rescaled as $t \to Kt$. The populations $\bar{N}_{1,2}$, $\bar{M}_{1,2}$ in the absorber medium have been normalized as $\bar{N}_1 \to \bar{N}_1 B_g l_g/\bar{Q}KL$, etc. After these renormalizations, the parameters α and β become

$$\alpha = \frac{B_a l_a \bar{Q}}{B_g l_g}, \quad \beta = \frac{B_a}{B_g}.$$

To the parameters of the 4:4 model, we assigned the values used in previous studies of CO_2 lasers. The data for the CO_2 molecules are taken from [43], whereas those for the saturable absorber SF_6 are found in Ref. [22].

In this model, the control parameters are taken to be Q and η (the cavity-frequency detuning), while α and β remain constant ($\alpha = 0.75$ and $\beta = 200\gamma$), unless otherwise stated. The numerical values of the parameters α and β have been taken from [11]. Interestingly, we find that the parameter values for which the instabilities arise in the 4:4 model have the same order of magnitude of those of the 4:2 model [51], which in the limit of a fast saturable absorber was studied in Ref. [11].

Following a reduction procedure [52,53], we obtain a reduced model (RM) from the CM in Eq. (2). This procedure, known as the *reduction principle*, is quite generally applicable [54]. The RM is obtained from the CM in Eq. (2) by first making a linear transformation to new coordinates. The old coordinates are the energy level populations in both the amplifier and the absorber. In the amplifier equations, the relaxation rates of two of the new variables are very large compared to those of the other two. As a result, we neglect their time derivatives. A similar situation occurs in the saturable absorber equations, except that another new variable decouples from the remaining equations because $\bar{\gamma}_1 = \bar{\gamma}_2 = \gamma$. The linear transformation is related to the eigenvectors of the trivial solution in Eq. (2), where $I = 0$. Using this transformation, the following equations are obtained:

$$\begin{aligned}
\frac{dI}{dt} &= I\left[-1 + \frac{(z+1)\Omega}{z}(w - v) + \frac{\alpha(\bar{z}+1)\bar{\Omega}}{\bar{z}}\Delta\right],\\
\frac{dv}{dt} &= \Omega I(w - v) - \gamma_1 v,\\
\frac{dw}{dt} &= \Omega I(v - w) - \gamma_2 w + z\gamma_2 Q,\\
\frac{d\Delta}{dt} &= -2\beta\bar{\Omega} I\Delta - \gamma\Delta - \bar{z}\gamma,
\end{aligned} \tag{3}$$

where

$$\Omega = \frac{z+1}{(z+1)^2 + 2zI/\gamma_R'}, \quad \bar{\Omega} = \frac{\bar{z}+1}{(\bar{z}+1)^2 + 2\bar{z}\beta I/\bar{\gamma}_R'},$$

and

$$\begin{aligned}
v &= \frac{zN_1 + zM_1}{z+1},\\
w &= \frac{zN_2 + zM_2}{z+1},\\
\Delta &= \frac{\bar{z}(\bar{N}_2 + \bar{M}_2 - \bar{N}_1 - \bar{M}_1)}{\bar{z}+1}.
\end{aligned}$$

These equations are similar to those obtained by Asquini and Casagrande [55], who applied the adiabatic elimination of the resonant energy levels in both the absorber and amplifier. The precision of our reduction procedure was recognized within the context of similar laser models [43–49], and will be demonstrated in Sec. III.

B. The cavity-frequency detuning effect

The cavity-frequency detuning from the resonant frequencies of both the amplifier and absorber has an important effect on the behavior of the laser [22,26]. Despite a number of experiments where the cavity-frequency detuning has been monitored, we are unaware of a functional dependence between this parameter and the 4:4 model or any other CO_2 molecular laser model. However, in the context of the 3:2 model, a dependence *ansatz* is given in Ref. [30]. Although it is not explicitly deduced from the standard laser model equations, it gives a good description of the experiment [30].

To understand how the equations of the 4:4 model generalize from the exact resonance case in order to take into account cavity-frequency detunings, we write down the laser equations for the amplitudes of the electric field and the polarizations induced by the amplifier and absorber within the optical cavity, as carried out for a class-B laser [56]. Equation (1) generalizes as follows:

$$\begin{aligned}\frac{dE}{dt} &= -\frac{K}{2}E + i(\omega-\omega_c)E - GP - \bar{G}\bar{P},\\ \frac{dP}{dt} &= -\gamma_\perp P + i(\omega-\omega_a)P - GE(N_2-N_1),\\ \frac{d\bar{P}}{dt} &= -\bar{\gamma}_\perp \bar{P} + i(\omega-\bar{\omega}_a)\bar{P} - \bar{G}E(\bar{N}_2-\bar{N}_1).\end{aligned} \tag{4}$$

The equations for E, P, and $\bar{P}$ in Eq. (4) are coupled to those for the populations of the resonant and nonresonant rotational energy levels in the amplifier and absorber in Eq. (1). Here, E is the complex field amplitude within the laser cavity, and P and $\bar{P}$ are the polarizations of the resonant rotational levels in the amplifier and absorber. As for the parameters, G is the field-matter coupling constant in the amplifier, and $\bar{G}$ is that of the absorber. Both G and $\bar{G}$ are real numbers. We let ω denote the frequency of the reference frame. ω_c is the cavity frequency, ω_a is the resonant atomic transition frequency in the amplifier, and $\bar{\omega}_a$ is that in the absorber.

The electric field E and the polarizations P and $\bar{P}$ are rewritten in polar coordinates as

$$E = \rho\exp(i\theta), \quad P = \mu\exp(i\psi), \quad \bar{P} = \bar{\mu}\exp(i\bar{\psi}).$$

In Eq. (4), the adiabatic elimination of the equations for μ and $\bar{\mu}$ is based on the fact that $\gamma_\perp$ and $\bar{\gamma}_\perp$ are the fastest relaxation rates. In addition, if we consider that

$$\frac{2G^2}{\gamma_\perp} = \frac{B_g l_g}{KL}, \quad \frac{2\bar{G}^2}{\bar{\gamma}_\perp} = \frac{B_a l_a}{KL},$$

we obtain the following equations from Eq. (4):

$$\begin{aligned}\frac{d\delta}{dt} &= \eta - \gamma_\perp\tan(\delta) - \frac{1}{4}(N_2-N_1)\sin(2\delta),\\ \frac{d\bar{\delta}}{dt} &= \bar{\eta} - \bar{\gamma}_\perp\tan(\bar{\delta}) - \frac{1}{4}(\bar{N}_2-\bar{N}_1)\sin(2\bar{\delta}),\end{aligned} \tag{5}$$

where $\eta = \omega_c - \omega_a$, $\bar{\eta} = \omega_c - \bar{\omega}_a$, $\delta = \theta - \psi$, and $\bar{\delta} = \theta - \bar{\psi}$. In Eq. (5), time, relaxation rates, and frequency detunings have been renormalized: $t \to Kt$, $\gamma_\perp \to \frac{\gamma_\perp}{K}$, $\bar{\gamma}_\perp \to \frac{\bar{\gamma}_\perp}{K}$, $\eta \to \frac{\eta}{K}$, and $\bar{\eta} \to \frac{\bar{\eta}}{K}$.

After applying the following four steps to Eq. (4), suitably coupled with the populations, we obtain a reduced model (RM). First, assume that $\bar{\gamma}_1 = \bar{\gamma}_2 = \gamma$, as in Eq. (3). Second, eliminate adiabatically not only the variables μ and $\bar{\mu}$ from Eq. (4), but also the variables δ and $\bar{\delta}$ in Eq. (5), since their relaxation rates are the fastest, $\frac{\gamma_\perp}{K} \gg 1$, $\frac{\bar{\gamma}_\perp}{K} \gg 1$. Third, apply variable normalization to this new equation, as in Eq. (2). This step determines the complete model (CM) with frequency detuning. This CM is formally obtained by implementing the following substitution in Eq. (2):

$$\begin{aligned}I(N_2-N_1) &\to I(N_2-N_1)\cos^2(\delta),\\ I(\bar{N}_2-\bar{N}_1) &\to I(\bar{N}_2-\bar{N}_1)\cos^2(\bar{\delta}).\end{aligned}$$

Finally, apply the reduction procedure to this CM, as in Eq. (3). As a result, we obtain a reduced model (RM) with cavity-frequency detuning which is formally identical to Eq. (3), but where the new parameters are the following:

$$\begin{aligned}\tan(\delta) &= \frac{\eta}{\gamma_\perp},\\ \tan(\bar{\delta}) &= \frac{\bar{\eta}}{\bar{\gamma}_\perp},\\ \Omega &= \frac{(z+1)\cos^2(\delta)}{(z+1)^2 + 2zI\cos^2(\delta)/\gamma_{R'}},\\ \bar{\Omega} &= \frac{(\bar{z}+1)\cos^2(\bar{\delta})}{(\bar{z}+1)^2 + 2\bar{z}\beta I\cos^2(\bar{\delta})/\bar{\gamma}'_R}.\end{aligned}$$

We are not aware that this RM and its CM version have been studied previously in the literature. Both of these models show the functional dependence between the cavity-frequency detuning within the context of the 4:4 model or any other CO_2 molecular laser model. The cavity-frequency detuning has been varied in several CO_2 LSA experiments [26,30,57].

III. THE DUAL FOUR-LEVEL MODEL AND ITS REDUCED VERSION: A COMPARISON

In this section, we compare the bifurcation structure of the CM and the RM in the case of exact resonance, $\eta = \bar{\eta} = 0$, as the incoherent pump Q changes. These models are described in Sec. II A. In both models, much of the interesting dynamics takes place in the neighborhood of a Hopf bifurcation, as the incoherent pump in the amplifier changes. In the CM and the RM, the trivial solution, for which $I = 0$, loses stability at a transcritical bifurcation, where it intersects with a nonzero stationary family, as typically occurs in LSA model s [11–13,15,18]. The value of Q at this bifurcation point, when $\eta = \bar{\eta} = 0$, is given by

$$Q_{tc} = 1 + \alpha,$$

in both models. Past Q_{tc}, one leg of the bifurcating family of nontrivial stationary solutions consists of unstable solutions until a Hopf bifurcation is reached, beyond which these equilibria are stable, as seen in Figs. 1(a) and 1(b) for the CM and the RM.

The numerical computations, carried out with AUTO [32], depend sensitively on how small I gets. For this reason, it is better to use a new variable c, where $I = e^c$. The trivial solution $I = 0$ then corresponds to $c = -\infty$. For the nontrivial stationary solutions, our bifurcation diagrams show the absolute value of c versus Q, while for periodic solutions of period T, the

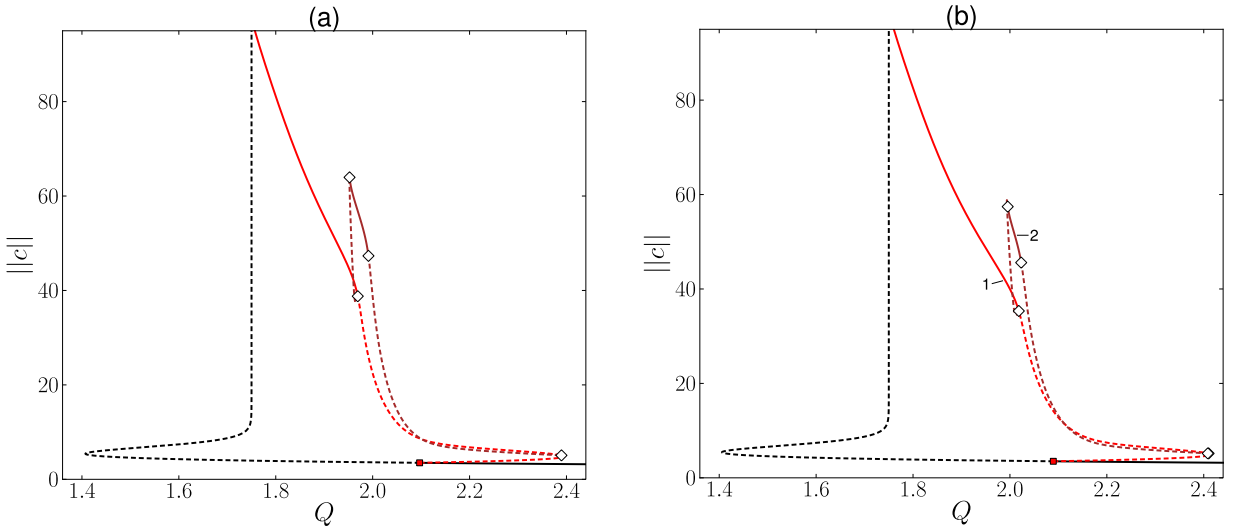

FIG. 1. (Color online) Bifurcation diagrams with stationary solution family (black) containing a Hopf bifurcation (solid red square), the bifurcating one-pulse family (red) containing two period doublings (PDs) denoted by open diamonds, and the bifurcating two-pulse family (brown) which contains two secondary PDs. Here, $\alpha = 0.75$, $\beta = 200\gamma$. Solid (dashed) curves denote stable (unstable) solutions. Isolas are omitted, but appear in Figs. 2 and 3. (a) Diagram for the CM. (b) Diagram for the RM, with the the one-pulse (two-pulse) families labeled 1 (2).

solution measure is defined as $||c|| \equiv \{\int_0^T [c(t)^2]dt\}^{1/2}/\sqrt{T}$. This choice of the solution measure is mostly dictated by the clarity of the bifurcation diagrams it produces. Note that due to the above transformation, the trivial solution cannot be seen in the bifurcation diagrams, as it corresponds to $||c|| = \infty$. In Secs. V and VI, we also use another solution measure, the L_2 norm, defined as $\{\int_0^T [\Sigma_{j=1}^N X_j(t)^2]dt\}^{1/2}/\sqrt{T}$, where $X_j(t)$, $j = 1,2,\ldots,N$, are the variables of the model, with $X_1(t) \equiv c(t)$.

The bifurcating nontrivial stationary solution family is stable to the right of the Hopf bifurcation point that it contains, as seen in Figs. 1 and 2. The remaining part of this family to the left of the Hopf point contains a fold and is unstable. Due to the choice of $||c||$ as the representative solution measure, the unstable part of the stationary family tends to infinity in the diagrams as it approaches $Q = 1.75$, where it bifurcates from the trivial stationary family $I = 0$.

The bifurcation diagrams for the CM and the RM displayed in Figs. 1– 3 also show the primary family of periodic solutions that emanates from the Hopf bifurcation. This family contains a fold as well as two period-doubling bifurcations (PDs), of which one is near the fold. The primary periodic solutions are stable beyond the second PD bifurcation. Note that the stable portion of the primary periodic family also tends to infinity in Fig. 1. The reason for this is that the periodic orbits along it approach a terminating orbit that is homoclinic to the trivial stationary solution $I = 0$. As a result of our choice of the solution measure $||c||$ for periodic solutions, this primary family then also approaches $||c|| = \infty$ in the diagram. In the 4:2 model for the CO_2 LSA, the homoclinic bifurcation curve

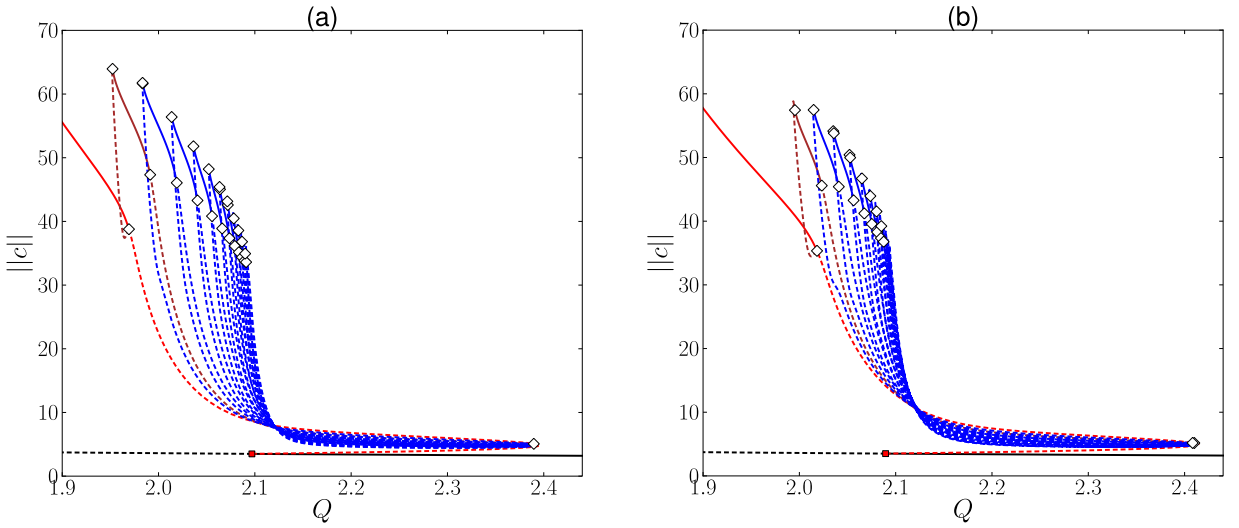

FIG. 2. (Color online) A closeup of Fig. 1, also showing the isolas. (a) Diagram for the CM. (b) Diagram for the RM. The stable regions (solid curves), from left to right, belong to the one-pulse family (red), the bifurcating two-pulse family (brown), and the the isolas $\mathcal{I}_3$–$\mathcal{I}_{13}$ (blue).

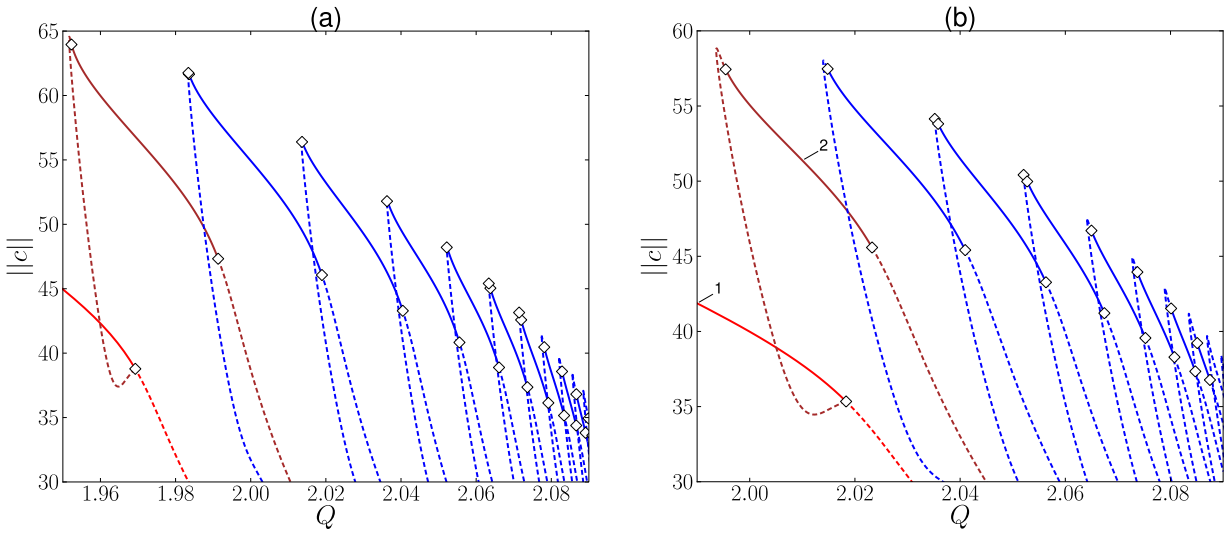

FIG. 3. (Color online) A further blowup of the bifurcation diagram in Fig. 2. The stable regions (solid curves), from left to right, belong to the one-pulse family (red), the bifurcating two-pulse family (brown), and the the isolas $\mathcal{I}_3$–$\mathcal{I}_{13}$ (blue). (a) Diagram for the CM. (b) Diagram for the RM, with the one-pulse (two-pulse) families labeled 1 (2).

emanates from a Bogdanov-Takens bifurcation, approaches the transcritical curve, and follows it exponentially closely [11], as also observed in Ref. [41] in a model for a semiconductor LSA without chaos.

Figures 1–3 also show that the two PD bifurcations along the primary family are connected by a single secondary periodic family, which contains a stability region bordered by further PD bifurcations. These secondary PDs can lead to more complicated stable dynamics that is typically confined to very small regions in parameter space. In these figures, $\Pi^{(2)}$ corresponds to the secondary periodic family which emanates from the primary periodic family $\Pi^{(1)}$.

Figure 2 shows that there are additional periodic solution families in the CM and the RM models that cannot be reached directly from the primary or secondary periodic families, at least not by only varying the parameter Q. Specifically, Fig. 2 shows a number of isolated families (isolas) of periodic PQS self-pulsations. We refer to these isolas as $\mathcal{I}_n$, $n = 3,4,5,\ldots$. The PQS self-pulsation $\Pi^{(n)}$ (MMOs) then belongs to the isola $\mathcal{I}_n$. In our figures, we only show $\mathcal{I}_n$ for $n = 3,4,\ldots,13$, although we have computed many more such isolas; in fact, there may be infinitely many. Figure 2 shows that several isolas $\mathcal{I}_n$ contain a region of stable PQS self-pulsations that is bordered by PDs. For the CM, the isolas $\mathcal{I}_3$ through $\mathcal{I}_{12}$ contain such a region, while for the RM, the isolas $\mathcal{I}_3$ through $\mathcal{I}_9$ contain a stable region. Of course these numbers also depend on other model parameters. In Ref. [13], we have shown that a small shift of a suitable parameter in the RM reproduces the

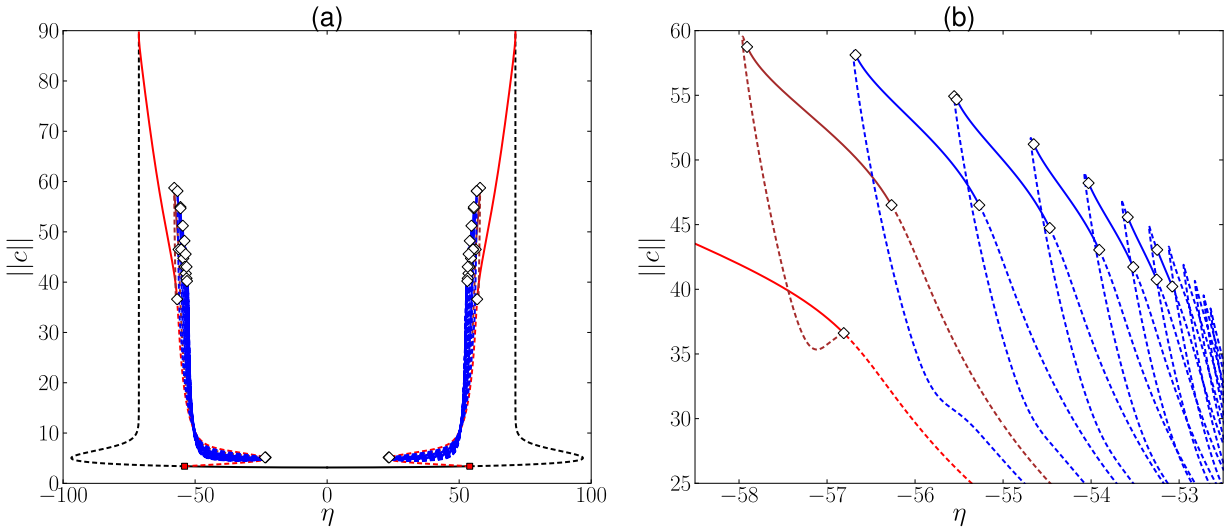

FIG. 4. (Color online) (a) Bifurcation diagram for the RM for $Q = 2.5$, $\alpha = 0.75$, $\beta = 200\gamma$, with a stationary family (black) containing two Hopf bifurcations (solid red squares), their bifurcating one-pulse families, period-doubled families, and isolas. (b) A closeup of the left part of (a). The stable regions, bordered by PDs (open diamonds), from left to right, belong to the one-pulse family (red), the bifurcating two-pulse family (brown), and the the isolas $\mathcal{I}_3$–$\mathcal{I}_{13}$ (blue).

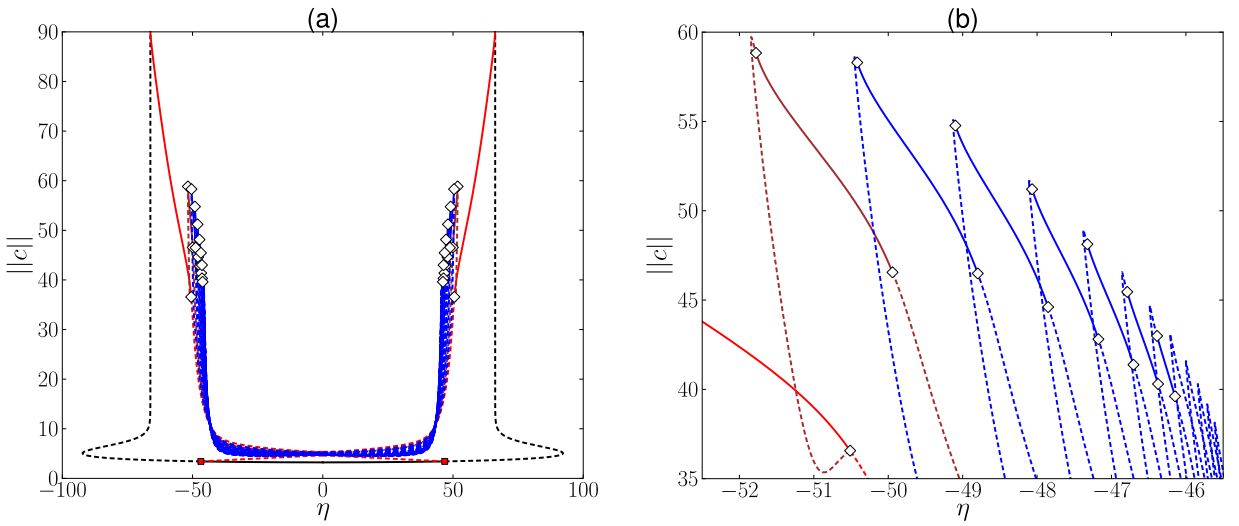

FIG. 5. (Color online) (a) As in Fig. 4(a), but for $Q = 2.4$, where the various families of periodic orbits have merged. (b) A closeup of the left part of (a).

sequence of stability intervals of the CM qualitatively well as Q changes.

The enlarged view of the stability regions in Fig. 3 shows more clearly that stable periodic solutions $\Pi^{(n)}$ coexist. For example, note the coexistence of stability regions along the primary periodic family (with label 1) and the period-doubled secondary family (labeled 2), as well as the coexistence of stable periodic orbits along the secondary periodic family and the isola $\mathcal{I}_3$.

We note the close qualitative similarity of the bifurcation diagrams of the CM and the RM, whose solution families play an important role in explaining observed physical phenomena such as period-adding cascades and chaotic behavior. We carried out an extensive comparison of the CM and the RM taking into account the cavity-frequency detuning effect, and here also we found that the bifurcation diagrams are very similar. For this reason, we will only discuss the bifurcation diagram for the RM in the following sections.

Our bifurcation diagram in Figs. 1–3 shows that period-adding cascades of PQS self-pulsations (MMOs), $\Pi^{(n)} \rightarrow \Pi^{(n+1)}$, or vice versa, occur within the framework of the 4:4 model. This disproves the common belief that the 4:4 model is unable to predict the $\Pi^{(n)}$ cascades observed in experiments [27,31].

IV. DEPENDENCE OF BIFURCATIONS ON LASER CONTROL PARAMETERS

In this section, we consider bifurcations in the CO_2 LSA system as the cavity-frequency detuning η changes. The results are for the RM of Sec. II B, for which the transition frequencies of both the amplifier and absorber are approximately the same. The laser frequency is assumed to be that of the optical cavity, whose length is subject to change. In the CO_2 LSA, where the absorber is a cell containing an SF_6 gas mixture, this situation holds for suitable energy levels [27,30]. As a result, we have $\eta = \bar{\eta}$ in what follows.

The fixed parameter values are $\alpha = 0.75$ and $\beta = 200\gamma$, while $Q = 2.5$ in Figs. 4(a) and 4(b), and $Q = 2.4$ in Figs. 5(a) and 5(b). Note the symmetry of the bifurcation diagrams with respect to $\eta = 0$, as seen in Figs. 4(a) and 5(a). As before, due to the choice of $||c||$ as the representative solution measure, the trivial solution family $I = 0$ is at $\eta = \pm\eta_{tc}$, where $||c|| = \infty$, and hence not visible in Figs. 4(a) and 5(a). However, as in Fig. 1 where Q is the free parameter, the bifurcating nontrivial stationary family (with $I > 0$) does appear in Figs. 4(a) and 5(a), where it tends to infinity as it approaches the point η_{tc} where it bifurcates from the trivial stationary family $I = 0$ as a result of a transcritical bifurcation. Here, $\eta_{tc} = \pm 71.30$ when $Q = 2.5$, and $\eta_{tc} = \pm 66.19$ when $Q = 2.4$. The nontrivial stationary solution family is stable between two symmetrically located Hopf bifurcations at $\eta_{HB} \approx \pm 53.99$ when $Q = 2.5$ [Fig. 4(a)], and at $\eta_{HB} \approx \pm 46.81$ when $Q = 2.4$ [Fig. 5(a)].

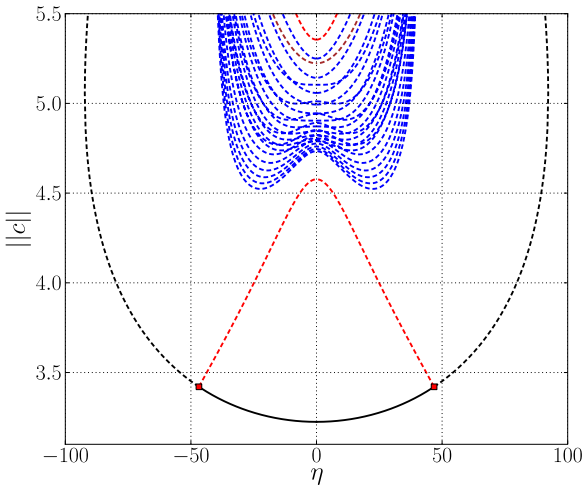

FIG. 6. (Color online) Closeup of Fig. 5(a), with stationary family (black) having two Hopf bifurcations (solid red squares), and a one-pulse family (dashed red) that connects the Hopf points. Also shown is the second, split one-pulse family, namely, the upper curve (also dashed red) at $\eta = 0$. The two-pulse family (brown) is the third curve from the top. The remaining curves are isolas (blue).

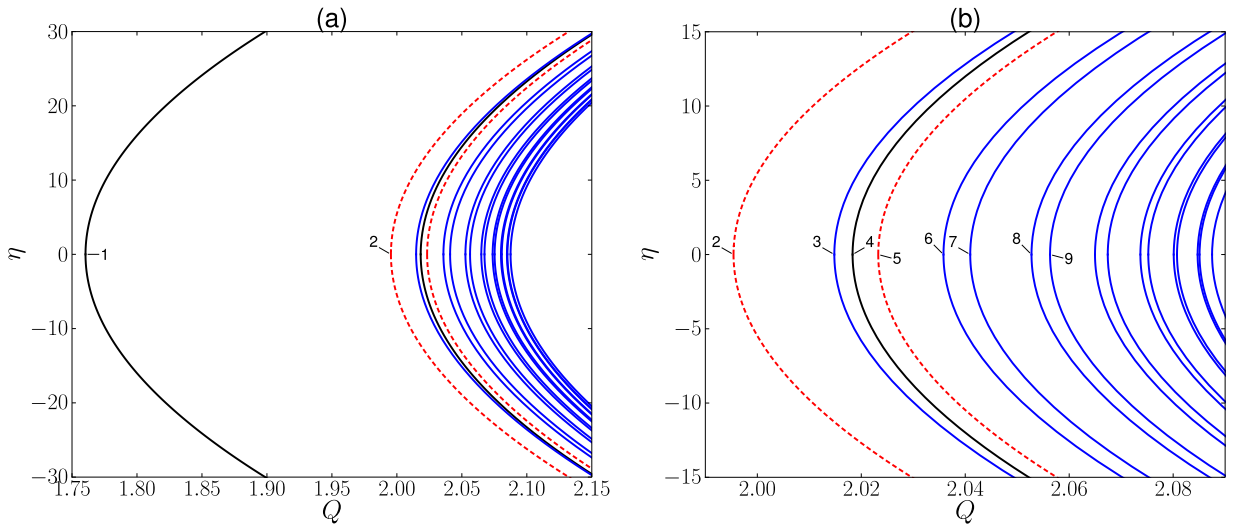

FIG. 7. (Color online) (a),(b) Loci of homoclinic orbits (curve 1; black), primary PDs (4; also black), secondary PDs (2, 5; dashed red), and PDs along the isolas (3, 6, 7, 8, 9, ...; blue), for $\alpha = 0.75$ and $\beta = 200\gamma$. The one-pulse solution family $\Pi^{(1)}$ is stable between curves 1 and 4, the period-doubled two-pulse family $\Pi^{(2)}$ is stable between 2 and 5, while the self-pulsations $\Pi^{(n)}$, $n = 3,4,\ldots$, are stable in overlapping regions, e.g., $\Pi^{(3)}$ between curves 3 and 7, and $\Pi^{(4)}$ between curves 6 and 8. (b) A closeup of (a).

The bifurcation diagram for $Q = 2.5$ in Fig. 4(a) also shows the families of periodic solutions that emanate from the two symmetrically located Hopf bifurcation points. Similar to the results in the preceding section, these families contain a fold and two PDs, of which one is near the fold. The periodic solutions are stable beyond the second PD at $\eta_{PD} \approx \pm 56.81$, as best seen in Fig. 4(b). As in the preceding section, these two PDs are connected by a single period-doubled family that, in turn, contains a stability region bordered by secondary PDs at $\eta \approx \pm 57.91$ and $\eta \approx \pm 56.27$; see Fig. 4(b). As also seen in Fig. 4(b), there are again isolas $\mathcal{I}_n$, of which the isolas $\mathcal{I}_3$–$\mathcal{I}_8$ contain regions of stable MMOs, referred to as $\Pi^{(n)}$, bordered by two PDs. Also note the coexistence of stable $\Pi^{(n)}$ for different n.

Figure 4(a) shows that there are no periodic orbits for $|\eta| < 22.69$. This is consistent with the fact that periodic orbits $\Pi^{(n)}$ do not exist for $Q = 2.5$ at exact resonance ($\eta = 0$), as seen in Fig. 2(b). However, Fig. 2(b) also shows that periodic orbits $\Pi^{(n)}$ do exist when $Q = 2.4$. Correspondingly, the bifurcation diagram in Fig 5(a), with Q fixed at $Q = 2.4$ and with η as bifurcation parameter, does have periodic orbits when $\eta = 0$. The transition from Fig. 4(a) (with $Q = 2.5$) to Fig. 5(a) (with $Q = 2.4$) can be explained by the merging of symmetry-related families, as their symmetry-related folds coalesce and annihilate each other. The enlarged view in Fig. 6 shows the periodic families when $Q = 2.4$, shortly after their merger. The values of η were changed in a recent experiment [30], where period-adding cascades and chaos were observed. However, it is difficult to say from these experimental results whether the latter was the case before or after the merging of the periodic families.

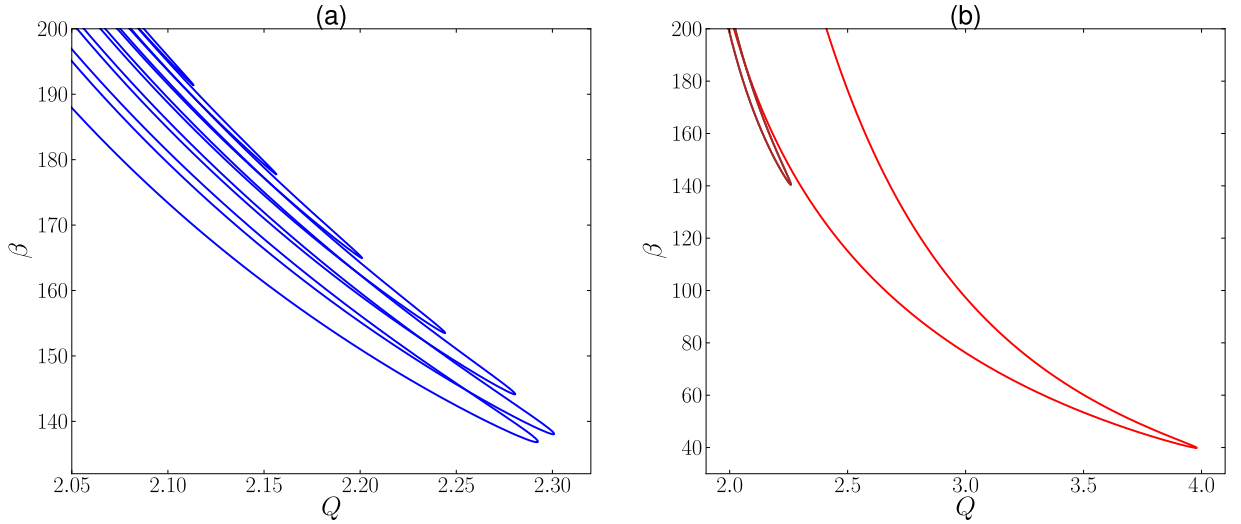

FIG. 8. (Color online) Loci of PDs for varying Q and β. (a) Loci of PDs along the isolas. The seven loci shown correspond, from bottom to top, to $\mathcal{I}_3, \mathcal{I}_4, \ldots, \mathcal{I}_9$. (b) The larger (red) locus represents PDs along the one-pulse family, and the smaller (brown) locus represents PDs along the two-pulse family. Fixed parameters are $\alpha = 0.75$, $\eta = 0$, $\gamma = 0.0065$.

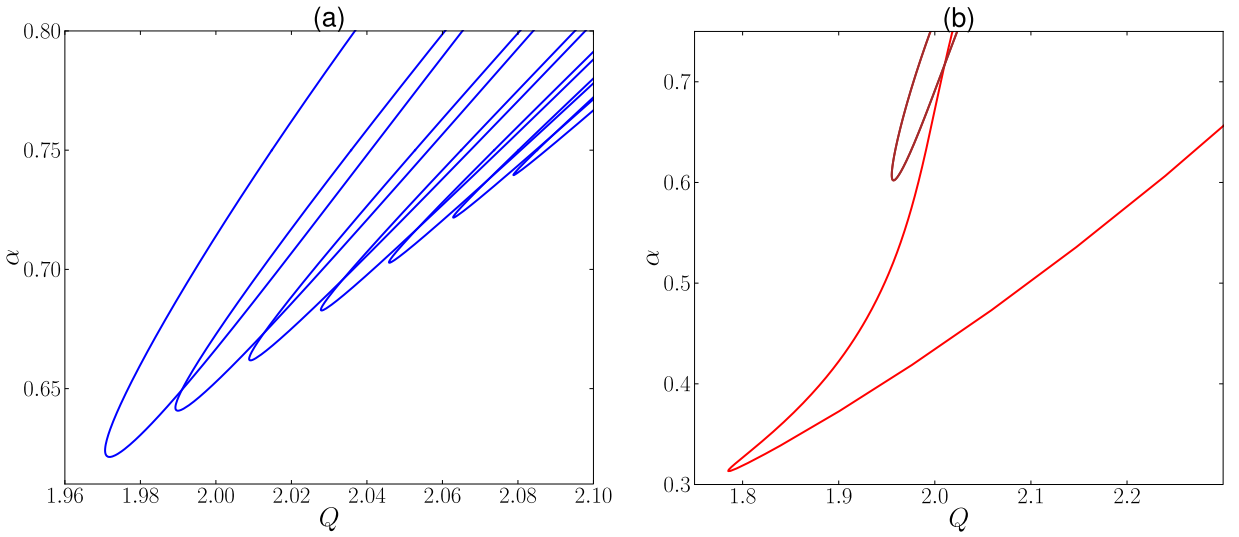

FIG. 9. (Color online) Loci of PDs for varying Q and α. (a) Loci of PDs along the isolas. The seven loci shown correspond, from bottom to top, to $\mathcal{I}_3, \mathcal{I}_4, \ldots, \mathcal{I}_9$. (b) The larger (red) locus represents PDs along the one-pulse family, and the smaller (brown) locus represents PDs along the two-pulse family. Fixed parameters are $\beta = 200\gamma$, $\eta = 0$.

Now consider the dependence of the Q intervals of stability on η, α, and β. Here, α accounts for the pressure or the equilibrium population difference in the absorber at $\eta = 0$, while β represents the saturability. These parameters have also been varied in experiments [26,31,57,58]. Figure 7 shows the locus of homoclinic orbits that terminates the primary periodic family of self-pulsations $\Pi^{(1)}$, and loci of PDs along the primary, secondary, and isola families, as dependent on Q and η. The locus of homoclinic orbits is the left-hand border of the stability region for the $\Pi^{(1)}$ self-pulsations. The loci of PDs are those that delimit stability regions. Note the parabolic shape of these curves. A similar dependence has also been observed in the experiments reported in Ref. [57], where the authors describe the stability regions of the periodic self-pulsations $\Pi^{(n)}$ as Q and η are changed.

The panels in Fig. 8 show the loci of PDs for varying parameters Q and β, where the latter is in units of γ. In particular, Fig. 8(a) shows that the Q intervals of stability of the isolas $\mathcal{I}_n$, bordered by PDs, shrink and disappear as β decreases. Note that for decreasing β, the isolas of higher n are the first to disappear, and that the effect of increasing β is to shift the Q interval of stability of $\mathcal{I}_n$ to the left. The latter is implicit in the synchronization of two unidirectionally coupled CO_2 LSA [58], where the output beam of the master LSA is injected into the saturable absorber of the slave LSA, inducing an effective increase in the parameter β in the latter. It implies that the Q interval of stability for a given attractor, say $\Pi^{(n)}$, shifts to the left in the slave LSA, precisely as observed in the experiment.

The Q intervals of stability of the primary periodic family $\Pi^{(1)}$ and those of the secondary period-doubled family $\Pi^{(2)}$ are shown in Fig. 8(b). The dependence of these stability regions on β and Q is qualitatively similar to that observed in experiments [31], where the authors report the stability regions of the primary periodic family, the secondary period-doubled family, and the periodic self-pulsations, $\Pi^{(n)}$, which correspond to intervals bordered by PDs in Figs. 8(a) and 8(b).

Figure 9 shows the dependence of the PDs that define the Q intervals of stability on the parameter α. In particular, we see that as α decreases, the stability intervals on the isolas $\mathcal{I}_n$ become smaller and disappear one after another. The isolas themselves have the same fate: they shrink in size and disappear sequentially as α decreases. We also observe that for fixed α, the stability regions along the isolas contract as n increases. The dependence of these stability regions on α is observed in Fig. 9(b) for the secondary period-doubled family. As for the primary periodic family, the Q interval of stability lies between $Q = 1 + \alpha = 1.75$ and the red curve in Fig. 9(b).

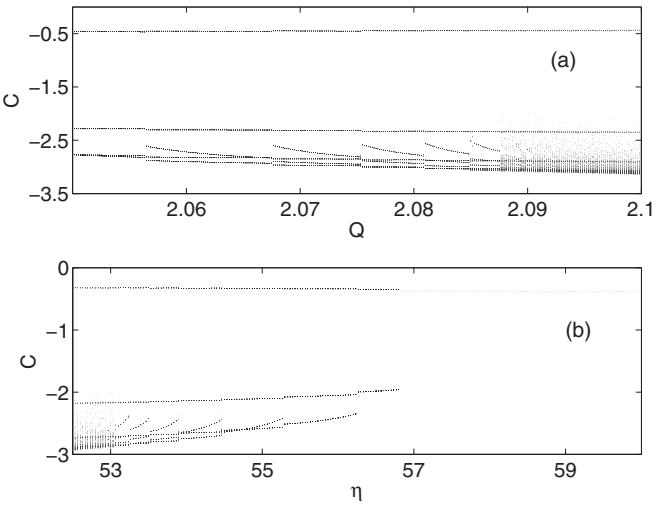

FIG. 10. (a) Plot of the Poincaré section, showing $c = \ln(I)$ vs increasing pump parameter Q for the 4:4 model (RM). This figure corresponds to the bifurcation diagram shown in Fig. 3(b). Here, $\alpha = 0.75$, $\beta = 200\gamma$, $\eta = 0$. (b) The Poincaré section, showing c vs decreasing cavity-frequency detuning η for the 4:4 model (RM). This figure corresponds to the bifurcation diagram shown in Fig. 4(b). Here $\alpha = 0.75$, $\beta = 200\gamma$, $Q = 2.5$. In both figures, we observe period-adding cascades and windows of chaotic behavior.

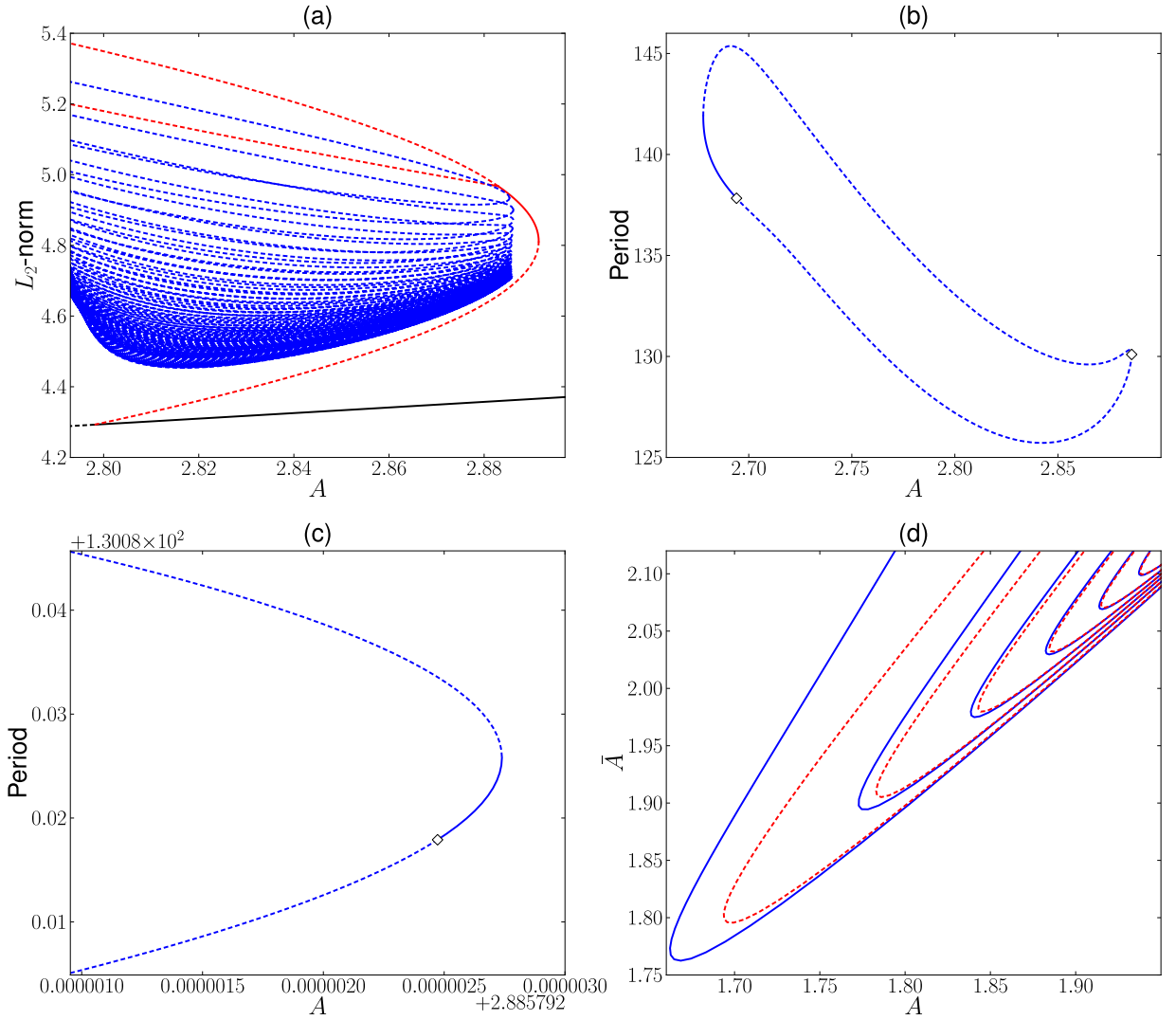

FIG. 11. (Color online) The 3:2 model. (a) Detail of the bifurcation diagram. The bottom (black) curve is a stationary family, the rightmost (red) curve is the $\Pi^{(1)}$ family, and the isolas $\mathcal{I}_n$, $n = 3,4,\ldots,50$, (blue) are the curves having folds near $A = 2.88$. Not indicated are PDs close to these folds. (b) The isola $\mathcal{I}_8$, with stability regions between PDs and folds. (c) A detail of the isola $\mathcal{I}_8$. (d) Loci of PDs (dashed red curves) and folds (solid blue curves) for $\mathcal{I}_3$–$\mathcal{I}_8$. The minimum of the fold curve for $\mathcal{I}_n$ is smaller than that for $\mathcal{I}_{n+1}$, and similarly for the PD curves. Fixed parameters are $\epsilon = 0.137$, $\bar{\epsilon} = 8.0$, $a = 4.17$, $b = 0.85$; while $\bar{A} = 3.50$ in panels (a)–(c).

The stability intervals of the isolas $\mathcal{I}_n$ of higher index n appear for larger Q, as seen in Fig. 2. In contrast, the stability intervals for higher index n arise for smaller absolute values of η, as seen in Figs. 4 and 5. This observation indicates that the dependence of the stability intervals shown in Fig. 9 is consistent with those of the experiments reported in Ref. [26], where α (absorber pressure) and η (cavity-frequency detuning) are changed.

Finally, to illustrate that chaos is present in the 4:4 model, we show in Fig. 10 the phase diagram as the control parameters are changed. The Poincaré section is taken at the maxima of $I(t)$. The windows of stability for the periodic orbits are consistent with those of Fig. 3 ($\eta = 0$) and Fig. 5 ($Q = 2.4$), as Q and η change. Our diagrams show that chaos is present in the 4:4 model, in contrast to previous studies [27,31] which suggested the absence of chaotic behavior in this model. In the next section, we show that the instabilities seen in Fig. 10 are induced by the presence of unstable periodic orbits in a neighborhood of a homoclinic tangency to an unstable periodic orbit.

V. BIFURCATION SEQUENCES NEAR A HOMOCLINIC ORBIT: A COMPARISON OF CO_2 LSA MODELS

A seminal article dealing with the study of instabilities near a homoclinic tangency to a periodic orbit is the mathematical work of Gavrilov and Shilnikov [59,60]. They proved that if a given two-dimensional map has a quadratic homoclinic tangency to a saddle periodic orbit at a parameter ρ, then there exists a sequence of parameter values $\rho_n^{(sn)} \to \rho$ such that at each value of $\rho_n^{(sn)}$, there is a saddle-node (SN) bifurcation creating orbits of period n. From Eq. (4.4) in Ref. [60], the following is obtained [61]:

$$\lim_{n\to\infty} \left(\rho_n^{(sn)} - \rho\right) = \frac{K_1}{(\lambda_u)^n}.$$

Here, λ_u denotes the unstable eigenvalue of the map and K_1 is a constant. In Ref. [60], a limit for $\rho_n^{(pd)}$ is shown to exist, where $\rho_n^{(pd)}$ is the PD where the stable periodic orbit born at $\rho_n^{(sn)}$ becomes a saddle. The resulting stability intervals are consecutive and disjoint. From Eq. (4.5) in Ref. [60], the following is obtained [61]:

$$\lim_{n\to\infty}\left(\rho_n^{(pd)}-\rho\right)=\frac{K_2}{(\lambda_u)^n},$$

for some constant K_2.

We assessed the validity of the conditions for these limits to hold as we change the pump parameter: Q in the 4:4 and 4:2 models [11,13] and A in the 3:2 model [12]. For completeness, we give the 3:2 and 4:2 models in the Appendix.

A. Homoclinic tangencies in the three LSA models

First we consider the 3:2 model [12]. The isolas $\mathcal{I}_n$ for this model are shown in Fig. 11(a) and the isola $\mathcal{I}_8$ is displayed separately in Fig. 11(b). The rightmost folds at $A_n^{(f)}$ tend to a limit $A^{(f)}$ as $n\to\infty$, where a homoclinic tangency to a saddle periodic orbit P occurs. P belongs to the primary family of periodic orbits that arises from a Hopf bifurcation. The rightmost and leftmost folds in Fig. 11(a) are SN bifurcations, as seen in Fig. 11(b) and its blowup in Fig. 11(c). The stability intervals near these folds are shown in a two-parameter diagram in Fig. 11(d). Based on the theory of Gavrilov and Shilnikov [60–62] and its multidimensional generalization [63], we find that the dependence of $|A_n^{(f)}-A^{(f)}|$ on the unstable eigenvalue λ_u, i.e., the unstable Floquet multiplier of P near the rightmost fold, holds to a good extent. As seen in Fig. 12(a), there is a region of linear behavior for the dependence of $\ln|A_n^{(f)}-A^{(f)}|$ on n, whose slope is to be compared to $-\ln(\lambda_u)$. The slope for the approximate straight line in Fig. 12(a) is -0.443, while $-\ln(\lambda_u)$ equals -0.438, where $\lambda_u=1.55$ is the unstable Floquet multiplier. $\lambda_{s1}=0.16$ and $\lambda_{s2}=6.0\times10^{-17}$ are the stable Floquet multipliers of the homoclinic tangency orbit P. This orbit is located near $A^{(f)}\approx 2.88$ on the lower part of the primary family in Fig. 11(a). Within the stability interval along $\mathcal{I}_n$ near the rightmost fold $A_n^{(f)}$, as shown in Fig. 11(c) for the isola $\mathcal{I}_8$, the $\Pi^{(n)}$ are *multiround*, stable periodic orbits, i.e., they make $n\geqslant 3$ rounds near the homoclinic tangency orbit P before closing up. The latter property allows for the coexistence of stable orbits $\Pi^{(n)}$ [63]. Small windows of typical chaotic behavior, as the incoherent pump changes, are more easily observed near the leftmost folds in the 3:2 model than in the 4:4 model, as suggested by Figs. 11(d) and 9(a): within these chaotic windows, no stability intervals along $\mathcal{I}_n$ exist.

The neighborhood of P, the unstable periodic orbit of homoclinic tangency, expands nearby volumes in the 4:2 and 4:4 models, in contrast to the 3:2 model. In such case, consider the backward flow [60], so unstable Floquet multipliers become stable, and conversely. The rightmost folds $Q_n^{(f)}$ of the isolas $\mathcal{I}_n$ for the 4:2 model when $\alpha=0.75$ are shown in Figs. 13(a) and 13(b), and for $\alpha=0.35$ in Figs. 13(c) and 13(d). For $\alpha=0.75$, the isola $\mathcal{I}_3$ is shown in Figs. 14(a) and 14(b) for the 4:2 and 4:4 models, respectively. In these figures, we see

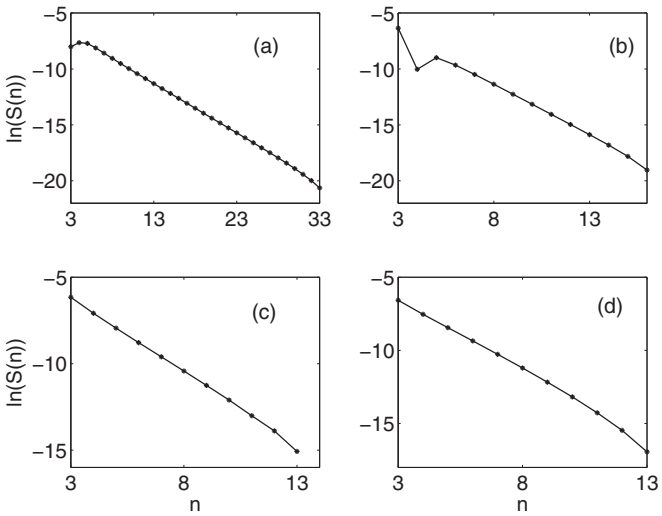

FIG. 12. (a) The 3:2 model: dependence of $S(n)=|A_n^{(f)}-A^{(f)}|$ on n, where $A_n^{(f)}$ is the pump parameter value for the rightmost fold of isola $\mathcal{I}_n$, and $A^{(f)}$ is the pump parameter value for the associated homoclinic tangency to the unstable periodic orbit P. Here, $\epsilon=0.137$, $\bar{\epsilon}=8.0$, $a=4.17$, $b=0.85$, and $\bar{A}=3.50$. (b) The 4:2 model: dependence of $S(n)=|Q_n^{(f)}-Q^{(f)}|$ on n, where $Q_n^{(f)}$ is the pump parameter value for the rightmost fold of isola $\mathcal{I}_n$ and $Q^{(f)}$ is the pump parameter value for the related homoclinic tangency to the unstable periodic orbit P. Here, $\alpha=0.35$, $\beta=200$. (c) The 4:2 model: similar to (b), but for $\alpha=0.75$, $\beta=200$. (d) The 4:4 model: similar to (b); dependence of $S(n)=|Q_n^{(f)}-Q^{(f)}|$ on n for the RM given in Eq. (3). Here, $\alpha=0.75$, $\beta=200\gamma$.

that there are no stability intervals in a neighborhood of the rightmost folds $Q_3^{(f)}$. Numerical results indicate that this holds for all right-hand folds at $Q_n^{(f)}$, whose index n is larger than a given integer n. The latter is congruent with the expansion of volumes near P in the 4:2 and 4:4 models. In these models, the $\Pi^{(n)}$ are multiround unstable periodic orbits, i.e., they make $n\geqslant 3$ rounds near the homoclinic tangency orbit P before closing up.

For the 4:2 model [11], an autonomous three-dimensional (3D) flow, we see in Figs. 12(b) and 12(c) that there is a region of approximate linear behavior for the dependence of $\ln|Q_n^{(f)}-Q^{(f)}|$ on n. The unstable and stable Floquet multipliers of the homoclinic tangency orbit P are $\lambda_u=6.12$ and $\lambda_s=0.40$ for $\alpha=0.35$, and $\lambda_u=183.28$ and $\lambda_s=0.44$ for $\alpha=0.75$. Considering the backward flow, the calculated value of $\ln(\lambda_s)$ is equal to -0.89 for $\alpha=0.35$, while the slope of the approximate straight line in Fig. 12(b) is also -0.89. Similarly, the calculated value of $\ln(\lambda_s)$ is equal to -0.82 for $\alpha=0.75$, while the slope of the approximate straight line in Fig. 12(c) is -0.86.

Finally, consider the 4:4 model, an autonomous 4D flow. In Fig. 12(d), there is a region of approximate linear behavior of the dependence of $\ln|Q_n^{(f)}-Q^{(f)}|$ on n. The unstable and stable Floquet multipliers of the homoclinic tangency orbit P are $\lambda_u=439.95$ and $\lambda_s=0.443\pm i0.057$, where the stable Floquet multipliers have a small imaginary part. As in the 4:2 model, we consider the backward flow. The calculated value of $\ln(|\lambda_s|)$ is equal to -0.80, while the slope of the approximate straight line in Fig. 12(d) is -0.96. For completeness, we show,

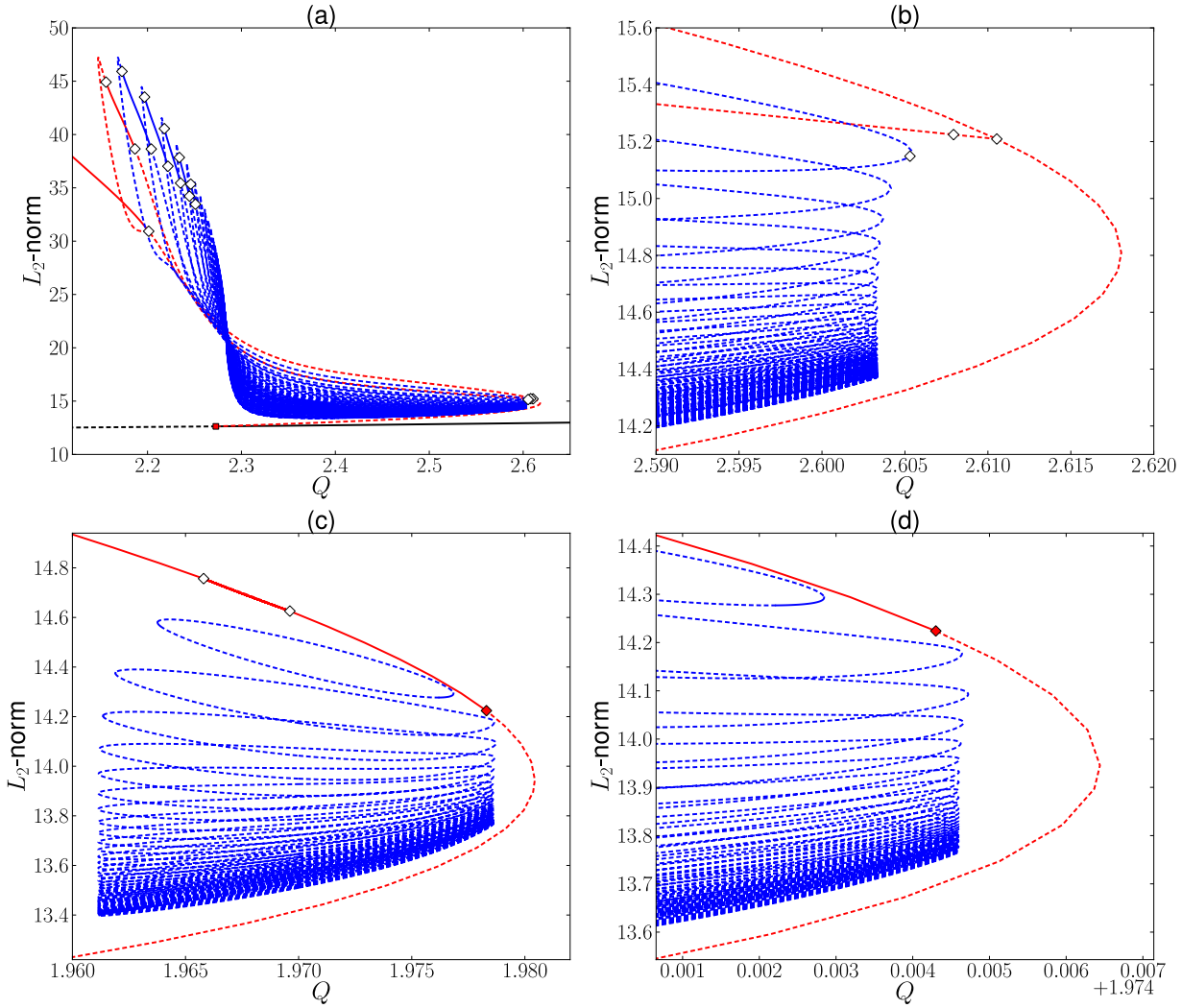

FIG. 13. (Color online) The 4:2 model. (a) Bifurcation diagram showing a stationary family (bottom, black) with Hopf bifurcation (solid, red square) from which the one-pulse family (red) bifurcates. The stable regions (solid curves) bordered by PDs (open diamonds), from left to right, belong to the one-pulse family (red), the bifurcating two-pulse family (also red), and the isolas $\mathcal{I}_3$, $\mathcal{I}_4$, $\mathcal{I}_5$, ... (blue). Here, $\alpha = 0.75$ and $\beta = 200$. (b) A detail of (a), showing the one-pulse family (rightmost curve, red), with bifurcating two-pulse family (also red), and the isolas. (c) Similar to (a), but for $\alpha = 0.35$, $\beta = 200$. The rightmost curve (red) is the one-pulse family, with torus bifurcation (solid, red diamond) and PDs (open diamonds). The closed curves (blue) are the isolas $\mathcal{I}_n$, $n = 3,4,\ldots,38$. (d) A closeup of (c).

in Table I, all Floquet multipliers, the value of the theoretical slope according to the theory [60–62], and the estimated slope. The estimated slopes, which fit the data to some extent in Fig. 12, were taken to minimize the standard deviation in a suitable set of points.

In these two molecular models, there are PDs very close to the left and right folds of the isolas, at least for $\mathcal{I}_n$ with small n and $\alpha = 0.75$. This is in addition to the other two PDs which border the aforementioned Q intervals of stability, as shown in Figs. 13(a) and 13(b) for the 4:2 and 4:4 models. Thus, such isolas $\mathcal{I}_n$ have four PDs. Near the left fold of these isolas, there are very small stability regions bordered by the fold and the near-fold PD. This is in contrast to the rightmost folds, as discussed in the preceding paragraph.

The absence of the Q intervals of stability at the rightmost folds, for the isolas $\mathcal{I}_n$ with large enough n, can perhaps be explained as follows. The two cases considered in the 4:2 model ($\alpha = 0.35$, $\alpha = 0.75$) lead to the situation where $|\lambda_u\lambda_s| > 1$ holds. This implies expansion of volumes near the homoclinic orbit, ruling out the emergence of stable periodic orbits in a neighborhood of the homoclinic tangency. However, the Floquet multipliers of the homoclinic tangency orbit P for the backward flow give a qualitatively good description of the slope dependence of $\ln|Q_n^{(f)} - Q^{(f)}|$ on n, as expected from the Gavrilov-Shilnikov (GS) theory, since volumes contract. The latter is similar in the 4:4 model, except that now we have a homoclinic tangency to a saddle-focus periodic orbit, where $|\lambda_u\lambda_s| > 1$, $|\lambda_u||\lambda_s|^2 > 1$. This implies again that in a neighborhood of the homoclinic orbit, the emergence of stable periodic orbits is inhibited.

Table I shows that the 3:2 model has a homoclinic tangency to the saddle periodic orbit P at $A^{(f)}$, where $|\lambda_u\lambda_{s1}| < 1$, $|\lambda_u\lambda_{s2}| < 1$, $|\lambda_u||\lambda_{s1}||\lambda_{s2}| < 1$. As a result, stable periodic orbits may exist in neighborhoods of the rightmost folds.

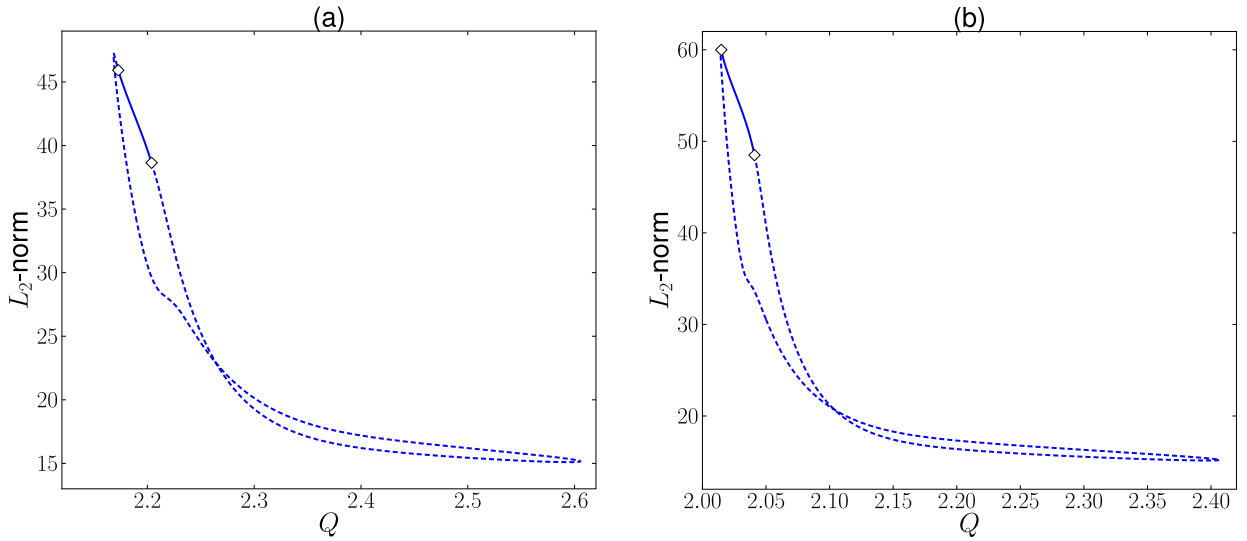

FIG. 14. (Color online) (a) The isola $\mathcal{I}_3$ of the 4:2 model, for which the periodic self-pulsations are stable (the solid blue segment) between two PDs (open diamonds). Here, $\alpha = 0.75$, $\beta = 200$. (b) The isola $\mathcal{I}_3$ of the 4:4 model (RM), for $\alpha = 0.75$, $\beta = 200\gamma$, $\eta = 0$.

In this multidimensional case [63], the Floquet multipliers satisfy the conditions for an infinite sequence of SN and PD bifurcations, and we verified the existence of these stability intervals for many I_n, $n \leqslant 50$ [12]. The saddle periodic orbit P is called sectionally or strongly dissipative since it has only one expanding eigenvalue (Floquet multiplier) and the product of any two eigenvalues has a norm of less than one. If this is not the case for P, then the unfolding of the homoclinic tangency can give infinitely many periodic orbits of smaller index such as saddles or sources [64], as in the 4:2 and 4:4 models. Finally, we point out that the genesis of isolas of periodic orbits in three-dimensional vector fields has been considered in Refs. [65,66]. Accordingly, a higher order codimension bifurcation analysis is necessary to determine the onset of the isolas.

VI. ISOLAS OF MIXED-MODE OSCILLATIONS IN THE CO_2 LASER WITH MODULATED LOSSES

In the 1980s, interest arose in the nonlinear dynamics of lasers with modulated parameters [15,18]. One of the first detailed experiments was done with a CO_2 laser with modulated losses (CO_2 LML) [67]. More recent studies found that the standard two-level model for this laser displays a network of self-similar stability islands [68]. This is also the laser we consider in this section, but within the framework of the four-level model. The four-level model, used to study the single-mode, homogeneously broadened CO_2 LML, describes transient and chaotic dynamics of this system [43–46,52]. Its validity has been supported by several studies [69,70]. At exact resonance between the laser cavity and the molecular transition frequencies, the coupled field-matter equations for the single-mode CO_2 LML are

$$\begin{aligned} \frac{dI}{dt} &= -[1 + \epsilon\cos(\nu t)]I + \frac{(z+1)\Omega}{z}(w - v), \\ \frac{dv}{dt} &= \Omega I(w - v) - \gamma_1 v, \\ \frac{dw}{dt} &= \Omega I(v - w) - \gamma_2 w + z\gamma_2 Q. \end{aligned} \tag{6}$$

The variables and parameter values for the amplifier in Eq. (6) are those of the 4:4 and 4:2 models, where now $K = 31.746$ for the parameters in Table II. As in Eq. (3), time has been normalized: $t \to Kt$. An intracavity electro-optic crystal induces a modulation in the cavity losses of the form $1 + \epsilon\cos(\nu t)$, as shown in Eq. (6) for the intensity I. Here, ϵ and ν are the depth and frequency of modulation [43,44], where $\nu = 0.019792$, corresponding to 100 kHz.

We started from a known nonzero stationary equilibrium at $Q = 1.12$, when the forcing amplitude ϵ is zero. This solution was continued (as a periodic orbit) to a representative nonzero value of the forcing amplitude, for which we used $\epsilon = 0.05$ and $\epsilon = 0.06$, respectively. The periodic response at the target value of ϵ was then continued, keeping ϵ fixed and allowing Q to vary, resulting in the lower blue curve in Fig. 15(a) ($\epsilon = 0.05$) and in Fig. 15(b) ($\epsilon = 0.06$). In each of these two cases, the basic periodic family is unstable between two PDs.

TABLE I. The Floquet multipliers, the value of the theoretical slope according to the theory, and the estimated slope.

Model	Floquet multipliers	Slope (theory)	Slope (data)
3:2 $A^{(f)} \approx 2.88$	$1.55; 1.0; 0.161; 6.0 \times 10^{-17}$	-0.43	-0.44
4:2 $Q^{(f)} \approx 1.97; \alpha = 0.35$	$6.12; 1.0; 0.407$	-0.89	-0.89
4:2 $Q^{(f)} \approx 2.60; \alpha = 0.75$	$183.2; 1.0; 0.445$	-0.82	-0.86
4:4 $Q^{(f)} \approx 2.40$	$439.95; 1.0; 0.443 \pm 0.057i$	-0.80	-0.96

TABLE II. Parameters and associated values for the 4:4,4:2 and LML models, see text.

Parameter	Value	Parameter	Value
γ_1	$0.08\ \mu/K$	$\bar{\gamma}_1$	γ
γ_2	$0.01\ \mu/K$	$\bar{\gamma}_2$	γ
γ_R	$z\gamma_R'$	$\bar{\gamma}_R$	$2.5\ \mu/K$
γ_R'	$0.7\ \mu/K$	$\bar{\gamma}_R'$	$0.0007\ \mu/K$
z	10	γ	$0.02\ \mu/K$
K	$3.2\ \mu$	$\gamma_\perp$	190
μ	$10^6\ \text{sec}^{-1}$	$\bar{\gamma}_\perp$	100

For example, when $\epsilon = 0.05$, the two PDs are at $Q = 1.107$ and $Q = 1.497$, as denoted by open diamonds in Fig. 15(a). The two PDs lead to a secondary family (red), which in turn is unstable between two secondary PDs. For example, in Fig. 15(a), these secondary PDs are located at $Q = 1.162$ and $Q = 1.271$. As seen in Fig. 15(a) ($\epsilon = 0.05$), the secondary PDs lead to a tertiary family that consists entirely of stable PD orbits. In contrast, in Fig. 15(b) ($\epsilon = 0.06$), the tertiary family contains further PDs.

Also seen in the two panels of Fig. 15 is an isola, represented by a closed curve (blue). The periodic solutions along the isola contain three maxima per period. In each of the two cases, $\epsilon = 0.05$ and $\epsilon = 0.06$, a stable starting periodic solution along the isola was found by time integration, and then followed by numerical continuation as the pump parameter Q is allowed to vary, thereby computing the entire isola including its unstable portions. Figure 15(a) for $\epsilon = 0.05$ shows that the isola contains two PDs connected by a secondary family (red) that consists entirely of stable orbits. Note that the stability intervals of both isolas in Fig. 15 are bordered by a SN and a PD. Similarly, for $\epsilon = 0.06$, the isola is unstable between two PDs connected by a secondary family (red). However, as seen in Fig. 15(b), this secondary family now contains a region of instability bordered by secondary PDs.

Figure 16(a) shows the locus of folds (blue) that delimit the isola, with ϵ as secondary parameter, the locus of PDs along the isola (red), and loci of secondary, tertiary, and quaternary PDs (also red). As seen in Fig. 16(a), the red PD loci quickly accumulate on a limiting curve. The interpretation of this figure includes the following: The isola does not exist for $\epsilon < 0.42$ (approximately). For increasing forcing amplitude ϵ, the set of primary PDs appears at $\epsilon \approx 0.049$, the secondary PDs appear at $\epsilon \approx 0.053$, the tertiary PDs at $\epsilon \approx 0.054$, etc. Stable periodic behavior of increasing complexity exists between consecutive red curves, while relatively simple stable behavior along the isola itself exists between the locus of folds (blue) and the first red locus (the primary PDs). Figure 16(b) shows a representative periodic orbit along a quaternary family for the isola with $\epsilon = 0.06$; this orbit has 24 maxima.

VII. CONCLUSIONS AND DISCUSSION

We have studied several models for the single-mode CO_2 laser with a saturable absorber (LSA), as well as a molecular model for the CO_2 laser with modulated losses (LML). We find that the bursting behavior of single-mode Q-switched CO_2 lasers is largely characterized by periodic mixed-mode oscillations organized along isolas, as either the incoherent pump parameter or the cavity-frequency detuning is varied. It would be interesting to determine if this solution structure is also present in other types of class-B lasers of physical relevance, such as Q-switched microchip lasers [71], where a recent model incorporates features of the 4:4 model from the CO_2 LSA. The existence in the amplifier of at least two effective energy levels (upper and lower) with slow dynamics but with different decay rates appears to be a necessary condition for the observation of isolas.

For the single-mode CO_2 LSA, we have studied the 4:4 model with physically relevant control parameters, and compared its salient features to those of two other single-mode CO_2 LSA models, namely, the 4:2 model and the 3:2 model.

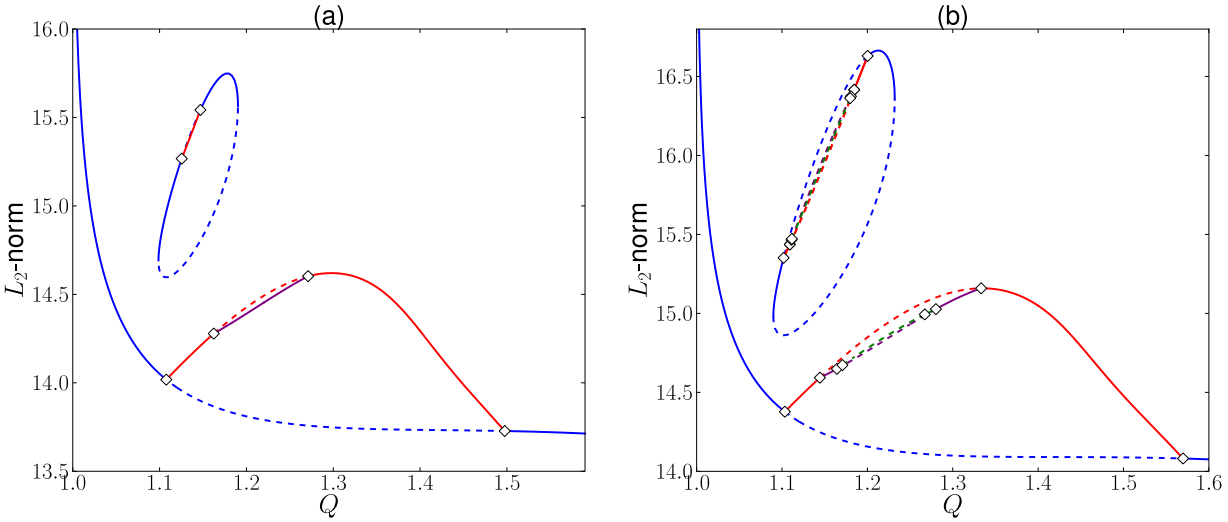

FIG. 15. (Color online) Bifurcation diagrams for (a) $\epsilon = 0.05$ and (b) $\epsilon = 0.06$, with $\nu = 0.019792$, $K = 31.746$. Solid (dashed) curves denote stable (unstable) orbits. In both diagrams, the lower (blue) curve is the main family, which is unstable (dashed) between two PDs connected by a secondary (red) family. The closed (blue) curve is an isola that also has two PDs connected by a secondary (red) family. For $\epsilon = 0.06$ in (b), there are further cascading PDs.

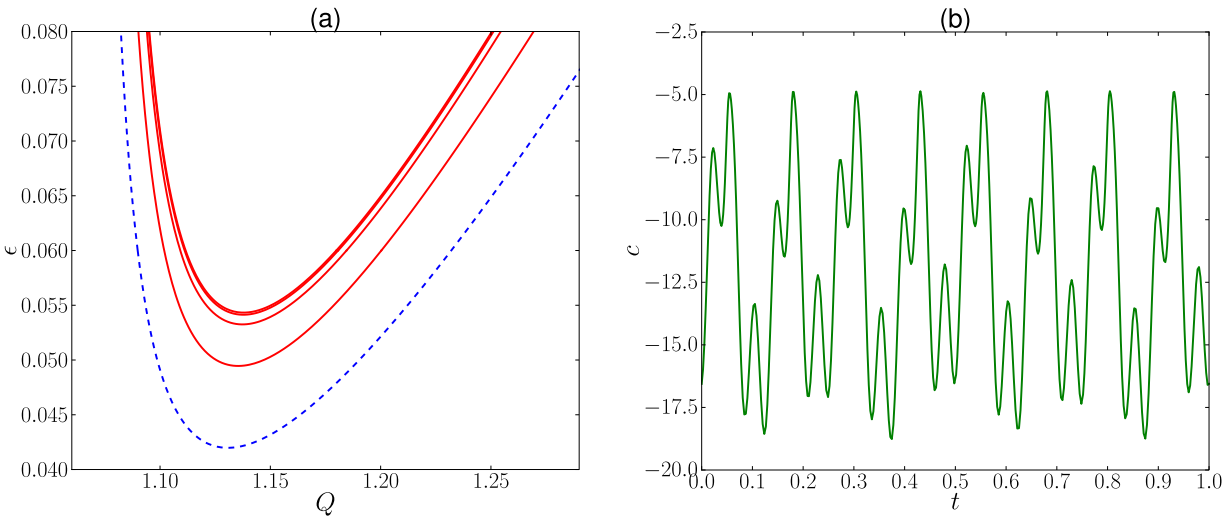

FIG. 16. (Color online) (a) The locus of folds (dashed blue) that delimit the isola, with Q and ϵ as parameters. Also shown are the loci of the first four cascading PDs (solid red), from bottom to top, for the isola. Note that there are only two PDs when $\epsilon = 0.05$, and at least eight when $\epsilon = 0.06$. (b) The value of $c = \log(I)$ vs scaled time for a stable quaternary solution for the isola for $\epsilon = 0.06$.

The 4:4 model was proposed more than three decades ago [21], and only now we find that its MMOs (periodic self-pulsations $\Pi^{(n)}$) are organized along isolas $\mathcal{I}_n$, as either the incoherent pump parameter Q or the cavity-frequency detuning η change. Stable MMOs along these isolas are delimited by PDs, with the stability interval decreasing in size as n increases. This organization of MMOs appears to be typical in these molecular models [11,13], where the sequence of coexisting stability intervals for different isolas $\mathcal{I}_n$ induces the phenomenon known as period-adding cascades. However, there is a difference depending on how the control parameters η and Q are changed. Specifically, due to the mirror symmetry of the bifurcation diagrams with respect to $\eta = 0$, symmetry-related families of periodic orbits may merge, provided that the symmetry-related folds coalesce at a critical value of Q. We are not aware of experiments in CO_2 LSA that either confirm or contradict this behavior.

Next we summarize relevant differences and similarities of the CO_2 LSA models. In the 3:2 model, it is assumed that the amplifier in the LSA is a three-level system with *ad hoc* parameters. Many studies show that it gives good agreement with experimental observations [23,24,27]. In contrast, in the 4:4 model, the amplifier is described by a refined four-level system [11,13,51], whose relaxation parameters have been physically estimated and later used in several experiments, as discussed in our paper. This description of the amplifier also explains experimental observations in the CO_2 LML [43,45,46]. Similar conclusions hold for the four-level model description of the absorber in the CO_2 LSA [22]. We have shown that the period-adding cascades induced by $\Pi^{(n)}$ and the associated windows of chaotic regime, as Q and η change, can be described within the framework of the 4:4 model. This is in contrast with the common belief [27,31] that the 4:4 model is unable to display these features observed in experiments. The coarse-grained bifurcation picture is qualitatively similar in the three models for the CO_2 LSA. However, they display distinct scenarios near a homoclinic tangency to a periodic orbit P as the pump parameter is allowed to vary.

In the 3:2 model, the rightmost folds of $\mathcal{I}_n$ accumulate at the pump parameter $A^{(f)}$ as $n \to \infty$, where the neighborhood of the saddle periodic orbit P at $A^{(f)}$ contracts volumes. The multidimensional GS theory [63] then holds, and stability intervals coexist for different $\mathcal{I}_n$. Considering that the $\Pi^{(n)}$ are multiround stable periodic orbits, infinitely many of them may coexist [63]. The latter would be an example of the effect known as the *Newhouse phenomenon* [64]. In the GS theory, the stable orbits are single round, making one round near the homoclinic tangency orbit before closing up, and the stability intervals are disjoint [61], while in our models the $\Pi^{(n)}$ are multiround.

In the 4:2 and 4:4 models, the rightmost folds of $\mathcal{I}_n$ accumulate at the pump parameter $Q^{(f)}$ as $n \to \infty$, where a neighborhood of the homoclinic tangency orbit P at $Q^{(f)}$ now expands volumes. The multidimensional GS theory [63] does not hold, and there are no stability intervals near these folds for $\mathcal{I}_n$ with large enough n. However, for the backward flow, which contracts volumes near P, the unstable Floquet multipliers become stable, and conversely, as $Q_n^{(f)} \to Q^{(f)}$, the GS rates hold to some extent. We note that in these two molecular models, the unstable orbits $\Pi^{(n)}$ are also multiround near the rightmost folds. In the four-level models, there is also a PD close to the rightmost folds, at least for $\mathcal{I}_n$ with small n, but no associated stability intervals were found. In the leftmost folds, where a nearby PD and the SN border a small stability interval, there is also a larger stability interval that is bordered by two additional PDs.

We found that the CO_2 LML also has MMOs organized along isolas as the pump parameter Q varies. A similar behavior is expected when the cavity-frequency detuning η is varied for suitable values of Q. The amplitude ϵ of the periodic modulation affects the stability intervals and the folds along the isolas. These stability intervals are bordered by SN and PD bifurcations.

For a possible experiment, we observe that as the incoherent pump changes, the relative position of the larger stability intervals along the isolas $\mathcal{I}_n$ is qualitatively different in the 3:2 model and in the molecular models; see Figs. 9(a) and 11(d). In particular, small windows of chaotic behavior are more easily observed in the 3:2 model, as the incoherent pump changes, compared to the molecular models. The number of these windows depends strongly on a second parameter such as the saturability [31] and the absorber pressure [12] in the 3:2 model and less in the molecular models. Moreover, merging of isolas is observed in the 4:4 model as the cavity-frequency detuning is changed from positive to negative for suitable values of the incoherent pump parameter. We are not aware of corresponding experiments. The fact that isolas are also present in the CO_2 LML makes this model a good candidate for further study, for example, of the dependence of the isolas on the driving frequency and the amplitude of the periodic losses.

ACKNOWLEDGMENTS

This work was supported by NSERC (Canada), the Instituto de Física, and VIEP at BUAP (México) and CONACYT (México).

APPENDIX: THE 3:2 AND 4:2 MODELS

The following set of equations defines the 3:2 model [12,27,30]:

$$\frac{dI}{dt} = I(U - \bar{U} - 1), \quad \frac{dU}{dt} = \epsilon[W - U(1 + I)],$$
$$\frac{dW}{dt} = \epsilon(A + bU - W), \quad \frac{d\bar{U}}{dt} = \bar{\epsilon}[\bar{A} - \bar{U}(1 + aI)],$$

where I is the laser intensity, and U and W are proportional to the active population difference and the effective population source term in the amplifier, respectively. $\bar{U}$ is proportional to the population difference in the absorber. The parameters ϵ and $\bar{\epsilon}$ are normalized relaxation rates in the amplifier and absorber. The constant a is proportional to the ratio of the absorption coefficient to the amplification coefficient. Finally, b is the squared ratio between two effective relaxation rates in the amplifier. The parameter A is proportional to the external incoherent pump rate in the gain medium, while $\bar{A}$ is proportional to the equilibrium population difference in the absorber. When A is the main control parameter, the numerical values assigned to the parameters in the 3:2 model are the following [27,30]: $\epsilon = 0.137$, $\bar{\epsilon} = 8.00$, $a = 4.17$, $b = 0.85$, and $\bar{A} = 3.50$. These values indicate that there is a fast variable, I, and two slow variables, U and W.

The 4:2 model [11,13] is given by the following equations:

$$\frac{dI}{dt} = I\left[-1 + \frac{(z+1)\Omega}{z}(w - v) - \frac{\alpha}{1 + 2\beta I}\right],$$
$$\frac{dv}{dt} = \Omega I(w - v) + \gamma_1 v,$$
$$\frac{dw}{dt} = \Omega I(v - w) - \gamma_2 w + z\gamma_2 Q,$$

where

$$\Omega = \frac{z+1}{(z+1)^2 + 2zI/\gamma_{R'}},$$
$$v = \frac{zN_1 + zM_1}{z+1},$$
$$w = \frac{zN_2 + zM_2}{z+1}.$$

The parameters and variables are the same as those of the 4:4 model, and Q is our main control parameter.

[1] M. Brons, T. J. Kaper, and H. G. Rotstein, Chaos **18**, 015101 (2008).
[2] M. Desroches, J. Guckenheimer, B. Krauskopf, Ch. Kuehn, H. M. Osinga, and M. Wechselberger, SIAM Rev. **54**, 211 (2012).
[3] J. Guckenheimer and C. Scheper, SIAM J. Appl. Dyn. Syst. **10**, 92 (2011); J. G. Freire and J. A. C. Gallas, Phys. Lett. A **375**, 1097 (2011); N. Baba and K. Krisher, Chaos **18**, 015103 (2008); M. Desroches, B. Krauskopf, and H. M. Osinga, *ibid.* **18**, 015107 (2008).
[4] B. Ermentrout and M. Wechselberger, SIAM J. Appl. Dyn. Syst. **8**, 253 (2009).
[5] E. Harvey, V. Kirk, M. Wechselberger, and J. Sneyd, J. Nonlinear Sci. **21**, 639 (2011); E. Harvey, V. Kirk, H. M. Osinga, J. Sneyd, and M. Wechselberger, Chaos **20**, 045104 (2010).
[6] F. Marino, M. Ciszak, S. F. Abdalah, K. Al-Naimee, R. Meucci, and F. T. Arecchi, Phys. Rev. E **84**, 047201 (2011); J. G. Freire and J. A. C. Gallas, *ibid.* **82**, 037202 (2010).
[7] M. Mikikian, M. Cavarroc, L. Couedel, Y. Tessier, and L. Boufendi, Phys. Rev. Lett. **100**, 225005 (2008).
[8] M. Higuera, J. Porter, and E. Knobloch, Chaos **18**, 015104 (2008).
[9] J. Guckenheimer, SIAM J. Appl. Dyn. Syst. **7**, 1355 (2008).
[10] M. Desroches, B. Krauskopf, and H. M. Osinga, Nonlinearity **23**, 739 (2010).
[11] Eusebius J. Doedel, Bart E. Oldeman, and Carlos L. Pando L., Int. J. Bifurcation Chaos **21**, 305 (2011).
[12] E. J. Doedel and Carlos L. Pando L., Phys. Rev. E **84**, 056207 (2011).
[13] Eusebius J. Doedel and Carlos L. Pando L., Int. J. Bifurcation Chaos **22**, 1250238 (2012).
[14] A. Penzkofer, Appl. Phys. B: Photophys. Laser Chem. **46**, 43 (1988).
[15] T. Erneux and P. Glorieux, *Laser Dynamics* (Cambridge University Press, New York, 2010).
[16] R. W. Hellwarth, Phys. Rev. Lett. **6**, 9 (1961).
[17] P. Mandel, *Theoretical Problems in Cavity Nonlinear Optics* (Cambridge University Press, New York, 1997).

[18] N. B. Abraham, P. Mandel, and L. M. Narducci, in *Progress in Optics XXV*, edited by E. Wolf (North-Holland, Amsterdam, 1988), Vol. 1.

[19] O. R. Wood and S. E. Shwarz, Appl. Phys. Lett. **11**, 88 (1967).

[20] I. Burak, P. Houston, D. Sutton, and J. Steinfeld, IEEE J. Quantum Electron. **7**, 73 (1971).

[21] J. Dupré, F. Meyer, and C. Meyer, Rev. Phys. Appl. (Paris) **10**, 285 (1975).

[22] E. Arimondo, F. Casagrande, L. Lugiato, and P. Glorieux, Appl. Phys. B: Photophys. Laser Chem. **30**, 57 (1983).

[23] M. Tachikawa, K. Tanii, M. Kajita, and T. Shimizu, Appl. Phys. B: Photophys. Laser Chem. **39**, 83 (1986); M. Tachikawa, K. Tanii, and T. Shimizu, J. Opt. Soc. Am. B **4**, 387 (1987).

[24] M. Tachikawa, F. L. Hong, K. Tanii, and T. Shimizu, Phys. Rev. Lett. **60**, 2266 (1988); M. Tachikawa, K. Tanii, and T. Shimizu, J. Opt. Soc. Am. B **5**, 1077 (1988).

[25] D. Hennequin, F. de Tomasi, B. Zambon, and E. Arimondo, Phys. Rev. A **37**, 2243 (1988).

[26] D. Dangoisse, A. Bekkali, F. Pappof, and P. Glorieux, Europhys. Lett. **6**, 335 (1988).

[27] M. Lefranc, D. Hennequin, and D. Dangoisse, J. Opt. Soc. Am. B **8**, 239 (1991).

[28] V. V. Nevdakh, O. L. Gaiko, and L. N. Orlov, Opt. Commun. **127**, 303 (1996).

[29] L. deB. Oliveira-Neto, G. J. F. T. da Silva, A. Z. Khoury, and J. R. RiosLeite, Phys. Rev. A **54**, 3405 (1996); P. C. deOliveira, M. B. Danailov, Y. Liu, and J. R. RiosLeite, *ibid.* **55**, 2463 (1997).

[30] H. L. D. de, S. Cavalcante, and J. R. Rios Leite, Chaos **18**, 023107 (2008).

[31] T. Tohei, M. Tachikawa, and T. Shimizu, Phys. Rev. A **45**, 5166 (1992).

[32] E. J. Doedel, B. E. Oldeman *et al.*, computer code AUTO-07P: *Continuation and Bifurcation Software for Ordinary Differential Equations* (Concordia University, Montréal, Canada, 2011), Version 0.8.

[33] F. Fernández-Sánchez, E. Freire, and A. J. Rodríguez-Luis, Dyn. Stab. Syst. **12**, 319 (1997).

[34] R. J. Olsen and D. G. Vlachos, J. Phys. Chem. A **103**, 7990 (1999).

[35] E. J. Doedel, *Continuation Techniques in the Study of Chemical Reaction Schemes*, Proceedings of the Special Year in Energy Mathematics, University of Wyoming, edited by K. I. Gross, (SIAM, Philadelphia, 1984), pp. 103–138.

[36] M. K. Stephen Yeung and S. H. Strogatz, Phys. Rev. E **58**, 4421 (1998).

[37] C. Bonatto and J. A. C. Gallas, Phys. Rev. E **75**, 055204(R) (2007).

[38] B. Krauskopf and S. Wieczorek, Physica D **173**, 97 (2002).

[39] W. Lauterborn and I. Eick, J. Opt. Soc. Am. B **5**, 1089 (1988).

[40] J. L. A. Dubbeldam, B. Krauskopf, and D. Lenstra, Phys. Rev. E **60**, 6580 (1999).

[41] J. L. A. Dubbeldam and B. Krauskopf, Opt. Commun. **159**, 325 (1999); A. Huber and P. Szmolyan, SIAM J. Appl. Dyn. Syst. **4**, 607 (2005).

[42] T. Erneux, P. Peterson, and A. Gavrielides, Eur. Phys. J. D **10**, 423 (2000); G. Kozyreff and T. Erneux, Eur. J. Appl. Math. **14**, 407 (2003).

[43] C. L. Pando L., R. Meucci, M. Ciofini, and F. T. Arecchi, Chaos **3**, 279 (1993).

[44] C. L. Pando L., G. A. Luna A., R. Meucci, and M. Ciofini, Phys. Lett. A **199**, 191 (1995).

[45] R. Meucci, M. Ciofini, and P. Y. Wang, Opt. Commun. **91**, 444 (1992).

[46] V. Zehnle, D. Dangoisse, and P. Glorieux, Optics Comm. **90**, 99 (1992).

[47] A. Varone, A. Politi, and M. Ciofini, Phys. Rev. A **52**, 3176 (1995).

[48] A. N. Pisarchik, R. Meucci, and F. T. Arecchi, Eur. Phys. J. D **13**, 385 (2001).

[49] F. T. Arecchi, L. Fortuna, M. Frasca, R. Meucci, and G. Sciuto, Chaos **15**, 043104 (2005).

[50] D. Sutton, I. Burak, and J. Steinfeld, IEEE J. Quantum Electron. **7**, 82 (1971).

[51] C. L. Pando L., Phys. Lett. A **210**, 391 (1996).

[52] M. Ciofini, A. Politi, and R. Meucci, Phys. Rev. A **48**, 605 (1993).

[53] P. Braza (unpublished).

[54] Y. Kuznetsov, *Elements of Applied Bifurcation Theory* (Springer-Verlag, New York, 2004).

[55] M. L. Asquini and F. Casagrande, Nuovo Cimento D **2**, 917 (1983).

[56] C. L. Pando L. and G. A. Luna A., Opt. Commun. **114**, 509 (1995).

[57] F. de Tomasi, D. Hennequin, B. Zambon, and E. Arimondo, J. Opt. Soc. Am. B **6**, 45 (1989).

[58] T. Sugawara, M. Tachikawa, T. Tsukamoto, and T. Shimizu, Phys. Rev. Lett. **72**, 3502 (1994).

[59] N. K. Gavrilov and L. P. Shil'nikov, Math. USSR (Sbornik) **17**, 467 (1972).

[60] N. K. Gavrilov and L. P. Shil'nikov, Math. USSR (Sbornik) **19**, 139 (1973).

[61] S. Wiggins, *Introduction to Applied Nonlinear Dynamical Systems and Chaos* (Springer-Verlag, New York, 2003).

[62] P. Gaspard and X.-J. Wang, J. Stat. Phys. **48**, 151 (1987).

[63] S. V. Gonchenko, I. I. Ovsyannikov, and D. V. Turaev, Physica D **241**, 1115 (2012).

[64] S. Newhouse, Topology **13**, 9 (1974); S. V. Gonchenko, D. V. Turaev, and L. P. Shilnikov, Russ. Acad. Sci. Dokl. Math. **47**, 410 (1993) [Doklady Akademii Nauk **329**, 404 (1993)]; J. Palis and M. Viana, Ann. Math. **140**, 207 (1994).

[65] P. Hirschberg and C. Laing, Physica D **89**, 1 (1995).

[66] A. R. Champneys and A. J. Rodríguez-Luis, Physica D **128**, 130 (1999).

[67] F. T. Arecchi, R. Meucci, G. Puccioni, and J. Tredicce, Phys. Rev. Lett. **49**, 1217 (1982).

[68] C. Bonatto, J. C. Garreau, and J. A. C. Gallas, Phys. Rev. Lett. **95**, 143905 (2005).

[69] T. J. Wang, Q. Y. He, J. Y. Gao *et al.*, J. Appl. Phys. **100**, 023121 (2006).

[70] W. Horbelt, J. Timmer, M. J. Bunner, R. Meucci, and M. Ciofini, Phys. Rev. E **64**, 016222 (2001).

[71] S. Han, H. H. Yu, H. J. Zhang *et al.*, IEEE Photon. Technol. Lett. **25**, 1785 (2013); H. H. Yu, Z. P. Wang, H. J. Zhang *et al.*, Appl. Phys. Express **10**, 102701 (2011).